AIAA AVIATION Forum
13-17 June 2016, Washington, D.C.
8th AIAA Flow Control Conference

Transonic Airfoil Performance Enhancement Using Co-Flow Jet Active Flow Control

Zixiang Liu* and Ge-Cheng Zha†
Department of Mechanical and Aerospace Engineering
University of Miami, Coral Gables, Florida 33124
E-mail: gzha@miami.edu

This paper performs a numerical proof of concept study to enhance transonic supercritical airfoil cruise performance using Co-Flow Jet(CFJ) active flow control technique. The Reynolds averaged Navier-Stokes(RANS) equations with one-equation Spalart-Allmaras turbulence model is used. A 5th order weighted essentially non-oscillatory(WENO) scheme with a low diffusion Riemann solver is utilized to evaluate the inviscid fluxes. A 4th order central differencing scheme matching the stencil width of the WENO scheme is employed for the viscous terms. Numerical trade studies are carried out to investigate the CFJ geometric effects on the performance enhancement. This research discovers that CFJ can significantly enhance the aerodynamic performance of RAE2822 transonic supercritical airfoil for both lift coefficient C_L and aerodynamic efficiency $(\frac{L}{D})_c$ that includes the CFJ pumping power. For the free-stream condition of M_∞=0.729, Re_∞=6.5×10^6, and AoA from 0° to 5.5°, the CFJ RAE2822 airfoil is able to achieve a performance enhancement with both C_L and $(\frac{L}{D})_c$ increased simultaneously by 18.7% and 14.5%, respectively at the peak aerodynamic efficiency point. At the maximum lift coefficient point, the CFJ airfoil is able to increase the C_L from 0.93 to 1.16 by 25.6% while slight decreasing the $(\frac{L}{D})_c$ from 21.3 to 19.6. Rigorous mesh refinement study is conducted to ensure solution convergence of the numerical results. Since the baseline airfoil drag is over-predicted by more than 30% due to the inadequacy of the RANS model, the predicted improvement of the CFJ airfoil tends to be on the conservative side. The unique feature of CFJ airfoil to augment lift and reduce drag at low energy expenditure is shown to be able to drastically improve the transonic airfoil cruise performance when the flow is benign at low AoA. The performance enhancement of CFJ transonic airfoil needs to be further proved by wind tunnel experiment as the next step. It is hoped that this research will open a door to significantly enhance transonic airfoil performance since the supercritical airfoil was invented in 1960's.

Nomenclature

V	Flow Velocity
ρ	Air Density
α, AoA	Angle of Attack
$\dot{m}$	Mass Flow Rate
M	Mach Number
M_i	Isentropic Mach Number
Re	Reynolds Number
L	Aerodynamics Lift
D	Aerodynamic Drag
p	Static Pressure
p_0	Total Pressure
P	Co-Flow Jet Required Pumping Power
η	CFJ Pumping System Efficiency

*Graduate Departmental Assistant, AIAA Student Member
†Professor, AIAA Associate Fellow

q_∞ Freestream Dynamics Head, $\frac{1}{2}\rho_\infty V_\infty^2$
C_L Lift Coefficient, $\frac{L}{q_\infty S}$
C_D Drag Coefficient, $\frac{D}{q_\infty S}$
C_M Moment Coefficient, $\frac{M}{q_\infty S c}$
C_p Pressure Coefficient, $\frac{p-p_\infty}{q_\infty}$
C_μ Jet Momentum Coefficient, $\frac{\dot{m}_j v_j}{q_\infty S}$
$(\frac{L}{D})$ Conventional Aerodynamic Efficiency
P_c Co-flow Jet Pumping Power Coefficient, $\frac{P}{q_\infty S V_\infty}$
$(\frac{L}{D})_c$ Corrected Aerodynamic Efficiency for CFJ Airfoil, $\frac{L}{D+P/V_\infty} = \frac{C_L}{C_D+P_c}$

Subscript
∞ Free Stream Conditions
$_j$ Jet Conditions

I. Introduction

I.A. Background

Since World War II, the breakthrough of turbo-jet engine technology and the increasing demand to travel globally within days have been pushing the commercial flight into transonic regime. Researchers first applied wing sweepback to overcome the onset of transonic drag rise and were able to reduce the critical Mach number to about 0.8.[1] Later in 1940's, manipulating airfoil shapes was another avenue to delay the drag rise in transonic regime. Several airfoil series such as NACA 1-series and NACA 6-series were developed, however those airfoils result in degradation of low speed performance.[2,3] Until early 1960's, the invention of supercitical airfoil by Whitcomb and his colleagues in NASA was considered to be the first successful effort to significantly extend drag-rise Mach number towards above 0.8 while maintaining excellent subsonic performance.[4] Following the appearance of supercritical airfoils, numerous of efforts had been put into the refinement of the supercritical airfoil design both experimentally and theoretically.[5] Also several successful flight tests(F-8,T-2C and F-111) demonstrated the applicability of supercritical airfoils. Ever since then, supercritical airfoils have been widely used in commercial aircraft as it is for transonic flight purpose. Few improvements of supercritical airfoil performance has been made in the past five decades.

With the belief that manipulation of the airfoil geometry has reached the limit, researchers have shifted attention to employ flow control with the hope to further improve the airfoil performance. There were attempts using porous upper surface near airfoil trailing edge to mitigate the transonic drag, which was found only to be able to decrease the Mach number slope of drag-rise while barely reducing any overall drag when Mach number is below 0.77.[6] Also efforts have been made to apply shock control bumps in order to mitigate the shock boundary layer interaction. Up to 20% drag was shown to be reduced at transonic speed. However, the shock control bump is mostly uncontrollable and it becomes detrimental to the aerodynamic performance at subsonic condition.[7,8] Active flow control method was also applied to supercritical airfoils to improve lift and aerodynamics efficiency only at takeoff and landing at low speed.[9,10]

Various active flow control techniques, including circulation-control(CC) airfoil, synthetic jet and plasma actuators flow control etc., have been proved to be effective to delay flow separation and increase the maximum lift coefficient at subsonic regime.[11] However, few flow control methods are able to improve lift and aerodynamic efficiency of transonic airfoil at transonic cruise condition when the flow is benign at low angle of attack. A flow control method that is able to enhance the transonic airfoil performance during both low speed takeoff-and-landing and cruise flight is thus appealing.

I.B. CFJ Active Flow Control

A zero-net mass-flux(ZNMF) active flow control technique developed by Zha et al.[12–21] is promising to achieve airfoil lift augmentation, drag reduction and stall margin increment at low energy expenditure.

In the CFJ airfoil concept, an injection slot near leading edge and a suction slot near trailing edge on the airfoil suction surface are created as sketched in Figure 1. A small amount of mass flow is withdrawn into the airfoil near the trailing edge(TE), pressurized and energized by a pumping system inside the airfoil, and then injected near the leading edge(LE) in the direction tangent to the main flow. The whole process

does not add any mass flow to the system and hence is a ZNMF flow control.

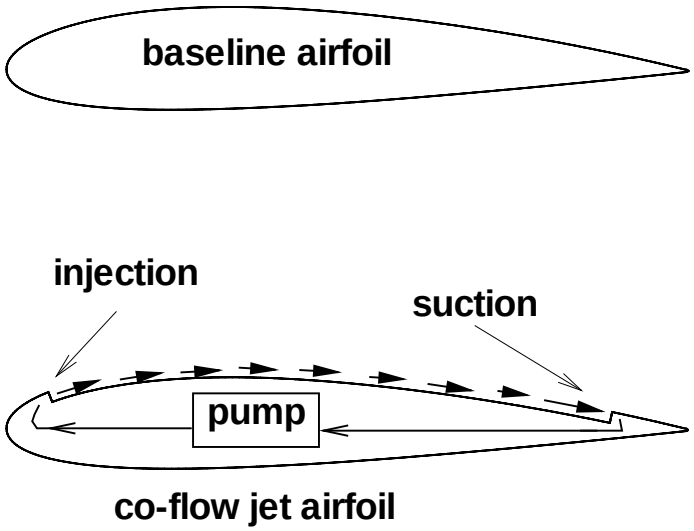

Figure 1: The sketch of a baseline airfoil and a CFJ airfoil.

The CFJ airfoil flow process provides a unique low energy expenditure mechanism, which has the injection near the suction peak of the airfoil where the lowest main flow pressure is located, and jet suction located near trailing edge where the highest main flow pressure is located. In other words, the required pumping energy is low since the low pressure makes the jet easy to be ejected out and high pressure makes the jet easy to be sucked in. The required pumping work of CFJ airfoil would be lower than those of the flow control methods injecting near trailing edge such as a CC airfoil. Dano et al.[18] and Lefebvre et al.[19] investigate the energy expenditure of the CFJ airfoil, which indicates that the CFJ airfoil gains more performance enhancement at higher Mach number due to compressibility effect and at higher angle of attack(AoA) due to lower energy expenditure. As pointed out by Zha et al.,[14] the injection and suction of CFJ airfoil are efficiently integrated and they both enhance boundary layer momentum and airfoil circulation.

The fundamental mechanism of CFJ airfoil is that the turbulent mixing between the jet and main flow makes a lateral transport of energy between the jet, boundary layer, and main flow to energize the wall boundary layer. The large vortex structures and adverse pressure gradient are all beneficial to enhance mixing. The energized boundary layer drastically increases the circulation, augments lift, and reduces the total drag or generates thrust(net negative drag).

With the superior performance of CFJ airfoil, Lefebvre and Zha[21] conducted a conceptual design of an electric CFJ general aviation(GA) airplane that achieves the wing loading 2-3 times higher than the conventional design. It means that the CFJ-GA airplane can reach a range of 2-3 times longer than a same size conventional GA. Lefebvre and Zha's work[21] also indicates for the first time that the CFJ airfoil can not only drastically increase stall AoA to achieve very high maximum lift coefficient, but can also obtain excellent cruise performance at low AoA when the flow is benign.

All the research previously done proving the effectiveness of CFJ airfoil is for subsonic flows. The purpose of this study is to demonstrate the capability of CFJ airfoil in transonic flow regime, aiming at developing a means to enhance the performance of transonic airfoil at cruise condition. It is hoped that

this research will open a door to significantly enhance transonic airfoil performance since the supercritical airfoil was invented in 1960's.

II. Methodology

II.A. Numerical Approach

The in-house high order accuracy computational fluid dynamics(CFD) code Flow-Acoustics-Structure Interaction Package(FASIP) is applied to conduct the numerical simulations. The Reynolds averaged Navier-Stokes(RANS) equations with one-equation Spalart-Allmaras(SA)[22] turbulence model is used for this research. The low diffusion E-CUSP scheme suggested by Zha et al.[23] and Roe's flux difference scheme[24] with the 5th order weighted essentially non-oscillatory(WENO) scheme proposed by Shen et al[25] are utilized to evaluate the inviscid fluxes. The conservative 4th order central differencing scheme suggested by Shen et al.[26] to match the stencil width of the 5th order WENO scheme is used for the viscous terms descritization. The implicit Gauss-Seidel(GS) line relaxation with two alternative sweeping direction in each time step is applied to achieve a fast convergence rate.[27] Parallel computing is implemented to save wall clock simulation time.[28] The code is extensively validated with various transonic flows including CFJ airfoil flows.[16,19,28–32]

II.B. CFJ Airfoil Parameters

II.B.1. Drag and Lift

The momentum exchange and pressure difference at the injection and suction slots produce reactionary force to the airfoil, which contribute to the total drag and lift. Through control volume analysis, Zha et al.[14] give the following formulations to calculate the lift and drag due to CFJ effect for CFD simulation

$$R_x = (\dot{m}_j V_{j1} + p_{j1} A_{j1})\ cos(\theta_1 - \alpha) - (\dot{m}_j V_{j2} + p_{j2} A_{j2})\ cos(\theta_2 + \alpha) \tag{1}$$

$$R_y = (\dot{m}_{j1} V_{j1} + p_{j1} A_{j1})\ sin(\theta_1 - \alpha) + (\dot{m}_{j2} V_{j2} + p_{j2} A_{j2})\ sin(\theta_2 + \alpha) \tag{2}$$

where x and y represent the drag and lift direction respectively, subscripts 1 and 2 stand for the injection and suction, θ_i $(i = 1, 2)$ is the angle between the injection or suction slot surface and the line normal to the airfoil chord, and α is the AoA, as shown in Figure 2.

The total drag and lift of the CFJ airfoil can then be expressed as below

$$D = F_x - R_x \tag{3}$$

$$L = F_y - R_y \tag{4}$$

where F_x and F_y are the drag and lift force due to surface integral of pressure and shear stress. The corresponding drag and lift coefficients are expressed as following

$$C_D = \frac{D}{\frac{1}{2}\rho_\infty V_\infty^2 S} \tag{5}$$

$$C_L = \frac{L}{\frac{1}{2}\rho_\infty V_\infty^2 S} \tag{6}$$

where ρ_∞ and V_∞ denote the free stream density and velocity. S is the wing planform area. For 2-D airfoil study, S denotes the planform area per unit span, which is equal to the airfoil chord length.

II.B.2. Jet Momentum

The jet momentum coefficient C_μ is a parameter used to quantify the jet intensity, which is defined as

$$C_\mu = \frac{\dot{m} V_j}{\frac{1}{2}\rho_\infty V_\infty^2 S} \tag{7}$$

where $\dot{m}$ is the injection mass flow rate, V_j is the averaged injection velocity at the injection slot opening.

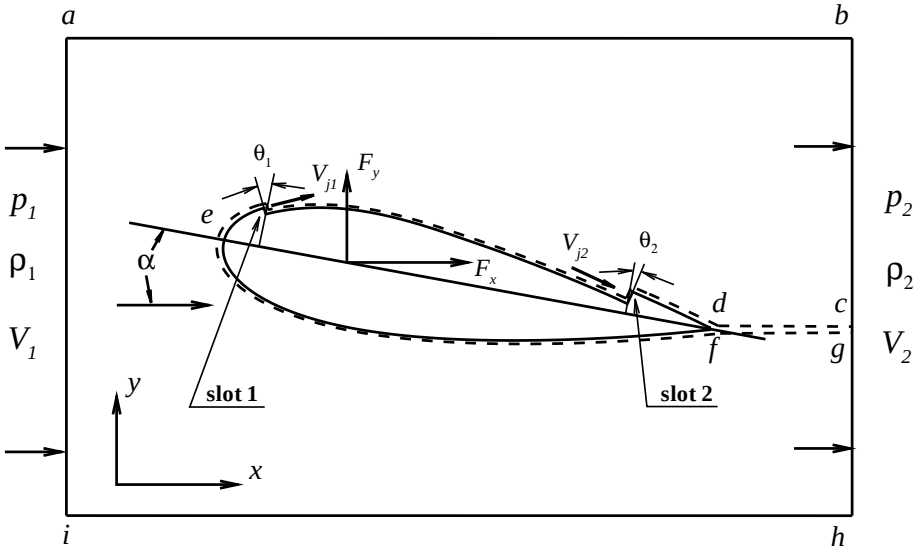

Figure 2: The CFJ airfoil control volume schematic.

II.B.3. Power Consumption

The CFJ can be implemented by mounting a pumping system inside the wing that withdraws air from the suction slot and blows it into the injection slot. The power consumption can be determined by the jet mass flow and total enthalpy change as following

$$P = \dot{m}(H_{01} - H_{02}) \tag{8}$$

where H_{01} and H_{02} are the total enthalpy in the injection cavity and suction cavity, respectively. P is the power required by the pump. Introducing the pump efficiency η and total pressure ratio of the pump $\Gamma = \frac{P_{01}}{P_{02}}$, the power consumption can be expressed as

$$P = \frac{\dot{m} C_p T_{02}}{\eta} (\Gamma^{\frac{\gamma-1}{\gamma}} - 1) \tag{9}$$

where γ is the specific heat ratio for air. The power consumption can be further normalized as a power coefficient as below

$$P_c = \frac{P}{\frac{1}{2}\rho_\infty V_\infty^3 S} \tag{10}$$

II.B.4. Aerodynamic Efficiency

The conventional airfoil aerodynamic efficiency is defined as

$$(\frac{L}{D}) = \frac{C_L}{C_D} \tag{11}$$

For the CFJ airfoil, the ratio above represents the pure aerodynamic relationship between lift and drag. To take account of the energy consumption of the CFJ, the conventional aerodynamic efficiency is modified by converting the power consumption into a corresponding drag force. The equation of the corrected aerodynamic efficiency is given as following[19]

$$(\frac{L}{D})_c = \frac{L}{D + \frac{P}{V_\infty}} \tag{12}$$

in which the pump power consumption P is converted into a force $\frac{P}{V_\infty}$ added to the aerodynamic drag D. The formulation above can be further expressed using the non-dimensional coefficients C_L, C_D and P_c as

$$(\frac{L}{D})_c = \frac{C_L}{C_D + P_c} \tag{13}$$

Note that when the pumping power is set to 0, $(\frac{L}{D})_c$ returns to conventional aerodynamic efficiency definition.

III. Results and Discussions

III.A. Validation and Mesh Refinement Study

The supercritical airfoil RAE2822 is chosen in the paper as the baseline airfoil for comparison. The RAE 2822 transonic airfoil has the maximum thickness of 12.1% at 37.9% chord and maximum camber of 1.3% at 75.7% chord. The computational parameters are selected based on the experiment Case 9 in the AGARD report,[33] which has the freestream conditions of Re_∞=6.5×10^6, M_∞=0.73, and α=3.19°. O-type structured grids with mesh size 255×55, 451×101, 641×101, 641×151 and 641×201 in circumferential and radial direction are utilized for mesh dependency study.

Figure 3 shows that the predicted airfoil surface pressure coefficient C_p distributions agrees very well with the experiment. The L_2 Norm convergence history in Figure 4 reveals that each computation cases are converged solidly to the steady state solution, reducing residual by at least 4 orders of magnitude after 10000 iterations. As shown in Table 1, the simulation using 641×151 mesh over-predicts the lift, drag and pitch moment correspondingly by 1.4%, 36.9% and 14.1%, respectively. This is speculated due to the inadequacy of RANS model to handle shock wave turbulent boundary layer interaction. The large drag coefficient deviation from the experiment is consistent with the RANS simulations of the same airfoil conducted by other research groups.[34,35] Table 1 indicates that the mesh of 641×151 and 641×201 are converged with the difference less than 1% for all coefficient of lift, drag and moment. The mesh of 641×151 is hence used for all the baseline airfoil study.

Furthermore, the CFJ airfoil with C_μ=0.005 under the same flow condition as the baseline airfoil is also simulated for mesh refinement study with mesh size of 451×101 and 641×151 being used. The aerodynamic coefficients and convergence history are shown in Table 2 and Figure 5, respectively. The mesh size of 451×101 and 641×151 are converged with the difference less than 1%. The mesh size of 451×101 is hence used for the CFJ airfoil study in this paper.

Even though the drag is over-predicted, it does not affect the merit of this study since what we seek is the trend with the consistent converged numerical simulation.

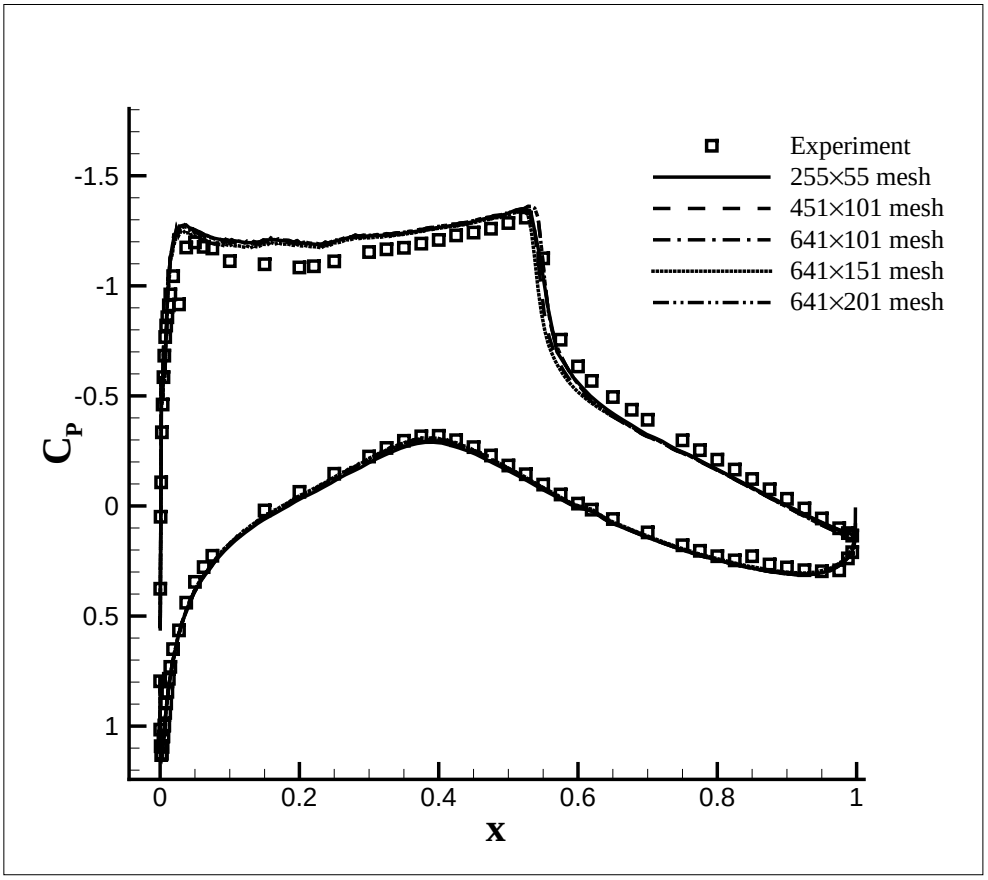

Figure 3: Comparison of pressure coefficient between simulation and experiment at M=0.729, $\alpha = 3.19°$.

Table 1: Baseline RAE2822 airfoil aerodynamics coefficients comparison between simulation and experiment.

Cases	C_L	C_D	C_M
Experiment	0.803	0.0168	-0.099
255×55 mesh	0.848	0.0232	-0.092
451×101 mesh	0.830	0.0224	-0.088
641×101 mesh	0.842	0.0225	-0.091
641×151 mesh	0.814	0.0230	-0.085
641×201 mesh	0.820	0.0232	-0.087

Table 2: CFJ airfoil aerodynamics coefficients comparison between different mesh sizes.

Cases	C_L	C_D	C_M	P_C
451×101 mesh	0.842	0.0155	-0.111	0.0028
641×151 mesh	0.848	0.0158	-0.112	0.0027

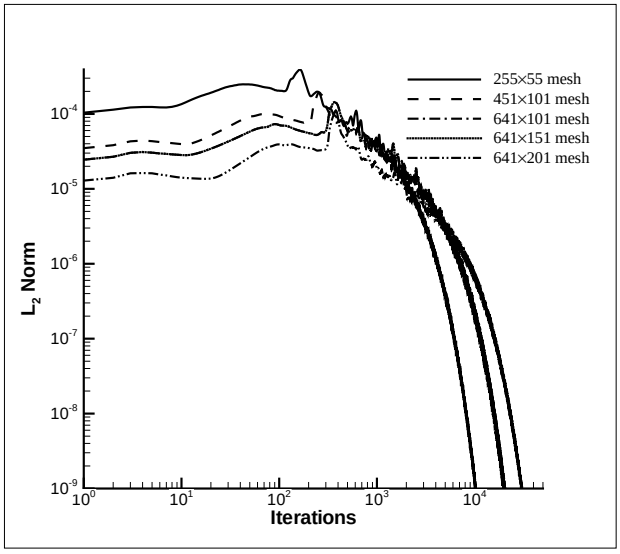

Figure 4: The convergence history of L_2 *Norm* relative error for the baseline RAE2822 airfoil cases.

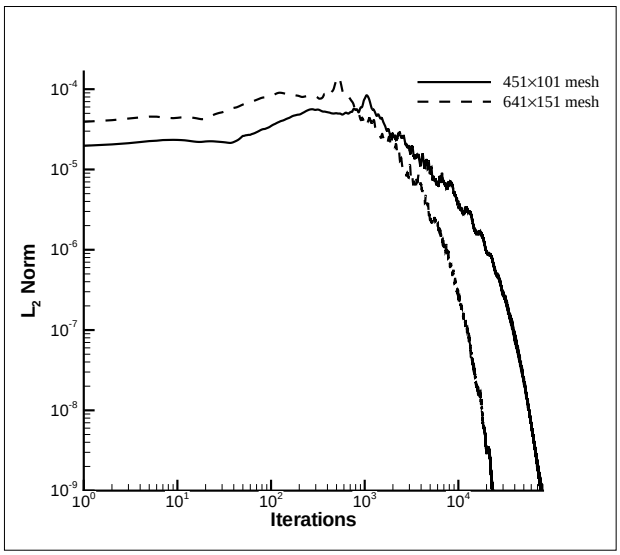

Figure 5: The convergence history of L_2 *Norm* relative error for the CFJ airfoil cases.

III.B. CFJ Transonic Airfoil Trade Study

For the CFJ transonic airfoil study, the same freestream conditions as the experiment with Re_∞=6.5×10^6 and M_∞=0.729 are used. The angle of attack ($\alpha = 2.31°$) that provides the baseline RAE2822 airfoil with the optimum aerodynamic efficiency ($\frac{L}{D}$) is simulated first as the reference point. As the initial configuration, the injection and suction slot width are both set to be 0.6% chord length, and the injection and suction slot location are 3% and 70% chord length, respectively.

III.B.1. Airfoil Suction Surface Translation

The previous subsonic CFJ[16,18,21,36] airfoil configurations create the injection and suction slots by translating the suction surface slightly downward. Such suction surface translation(SST) may not affect subsonic flows much, but appears to be very sensitive in transonic regime to affect the shock position and the airfoil performance.

A study concerning the effect of CFJ airfoil SST on its aerodynamic performance is carried out. CFJ RAE2822 airfoil configurations with SST from 0.0% to 0.6% chord length are studied. The schematics of some typical SST(0.0%, 0.1% and 0.6%) configurations are shown in Figure 6. The 0.0% SST means that the majority of the suction surface is not translated and remains the same as the baseline airfoil, but the local geometry close to the injection and suction slot is shaped to guide the flow tangential to the local airfoil surface.

Figure 7 demonstrates the lift coefficient C_L, drag coefficient C_D , power coefficient P_C and corrected aerodynamic efficiency $(\frac{L}{D})_c$ variation with different SST configurations and C_μ varying from 0.001 to 0.005. As C_μ increases, 0.1% SST airfoil yields the best aerodynamic performance in terms of both $(\frac{L}{D})_c$ and C_L. Compared with 0.0% SST airfoil, 0.1% SST airfoil exhibits almost the same C_L but substantially lower C_D. Given power coefficient P_C for both cases are with little difference, the 0.1% SST airfoil is selected for its high C_L and $(\frac{L}{D})_c$.

Figure 8 shows the Mach number contour around the airfoil. Figure 9 depicts the corresponding airfoil surface pressure and Mach number distributions. The CFJ cases with C_μ=0.003 are chosen for comparison. For the 0.6% SST configuration, the shock wave occurs significantly closer to the leading edge(LE) than the baseline and the 0.1% SST configuration. The large thickness reduction reduces the suction surface expansion, which leads to lower peak Mach number and hence produces less lift. The pressure distributions in Figure 9 also clearly show the low lift formation of the 0.6% SST case. It can be also observed that both the 0.0% SST and 0.1% SST CFJ airfoil cases generate greater supersonic regions with higher peak Mach number than the baseline airfoil, because the CFJ induces more expansion on suction surface. This clearly indicates that the CFJ is a very effective method to enlarge the supersonic region of a supercritical airfoil. However, as shown in Figure 9, the 0.1% SST case maintains the shock wave Mach number below 1.3, which avoids the high entropy and wave drag rise shown in the 0.0% SST case.

The CFJ transonic airfoil study hereafter will therefore employ the 0.1% SST configuration.

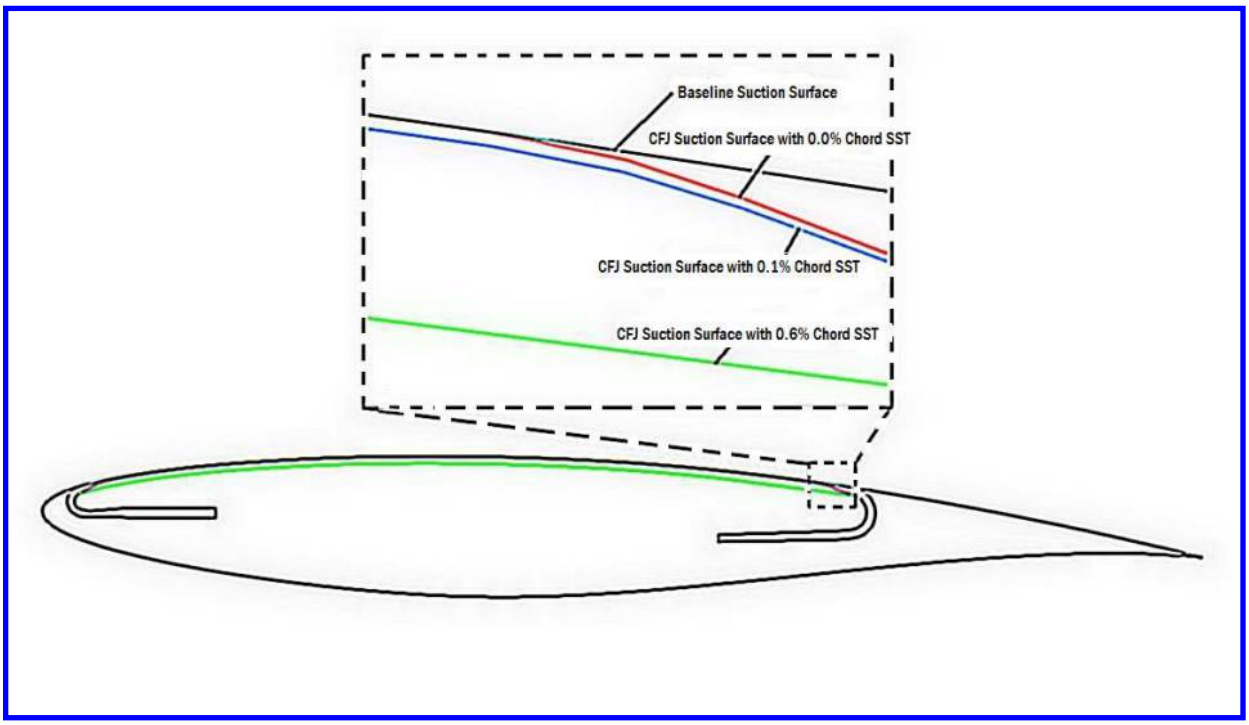

Figure 6: The CFJ transonic airfoils with different SST configurations.

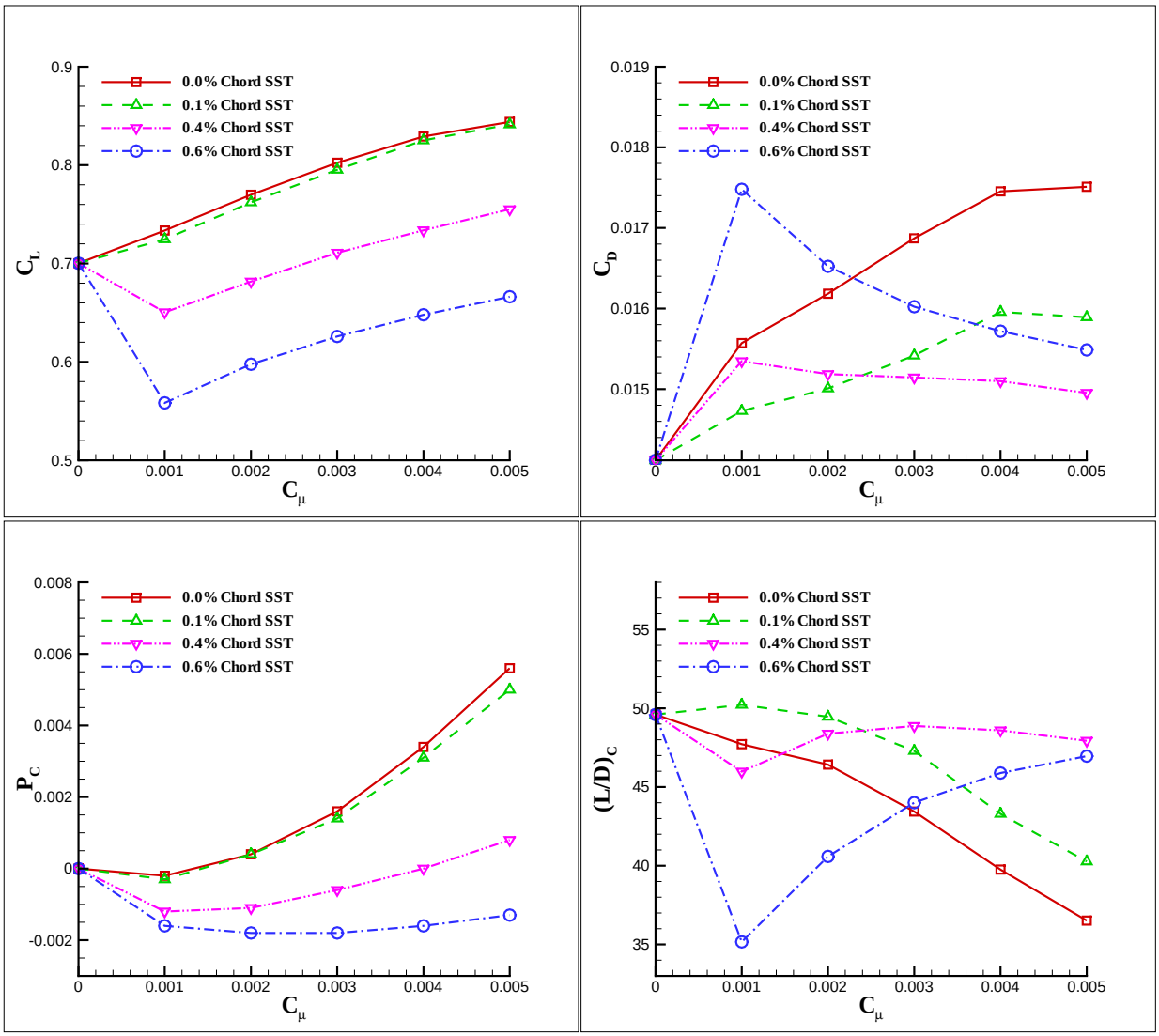

Figure 7: Lift coefficient C_L, drag coefficient C_D and corrected aerodynamic efficiency $(\frac{L}{D})_c$ for different SST configurations with C_μ varying from 0.001 to 0.005.

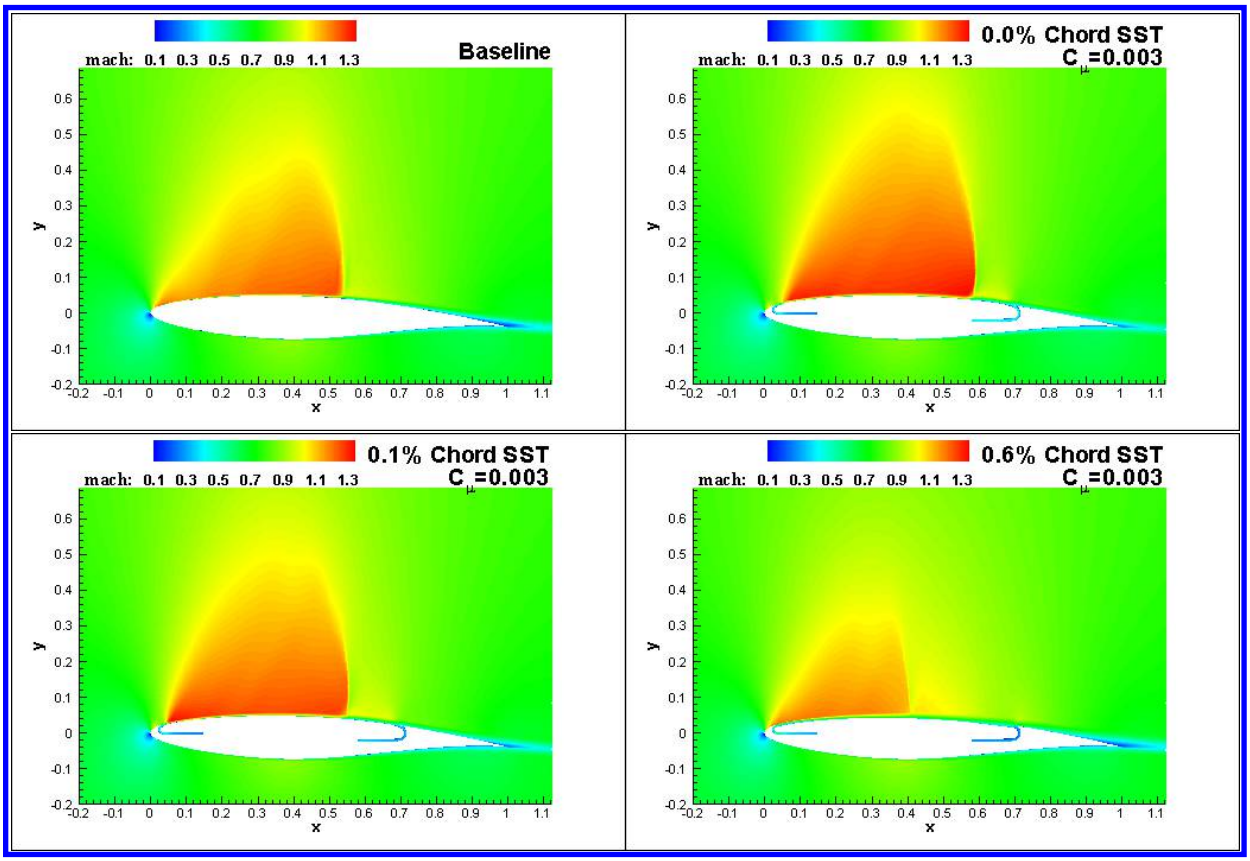

Figure 8: Mach number contours for the baseline airfoil and CFJ airfoils with different SST configurations at $C_\mu = 0.003$.

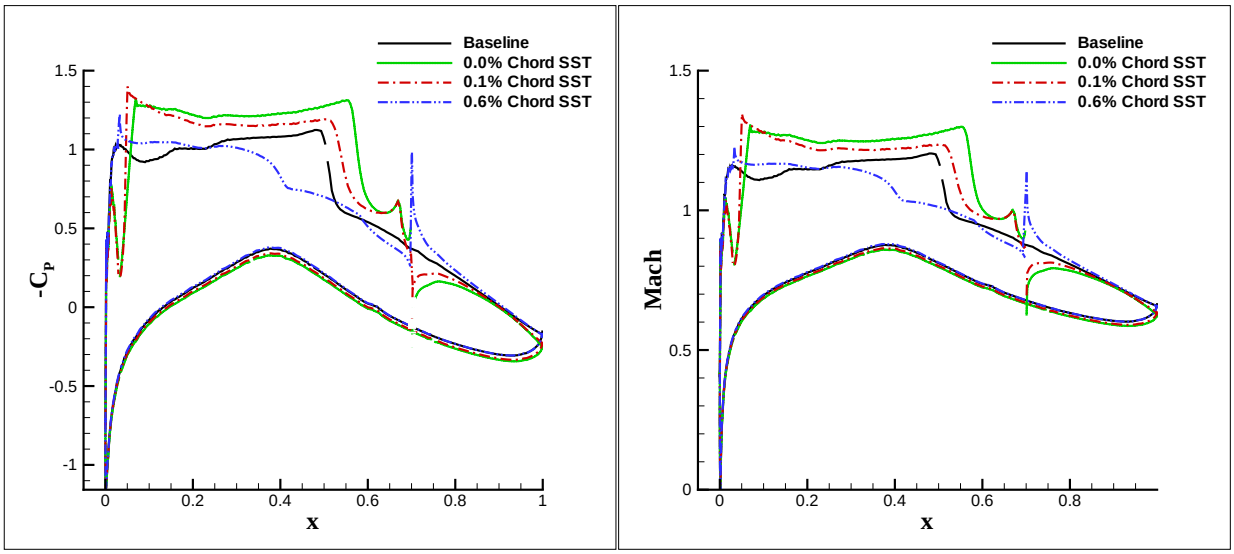

Figure 9: Airfoil surface pressure and Mach number distributions for the baseline airfoil and CFJ airfoils with different SST Configurations at $C_\mu = 0.003$.

III.B.2. CFJ Suction Slot Opening Angle

The previous subsonic CFJ airfoil designs[16,18,21,36] create the suction slot opening mostly normal to the local suction surface. Under this condition, the suction slot reactionary force contributes significantly to the drag due to ram effect as indicated by Equation (1) and Equation (2).

The CFJ suction ram drag is at a similar order of magnitude to the overall drag at low C_μ. Therefore, it is beneficial to have the suction slot more perpendicular to the airfoil upper surface with the slot angle θ_2 closer to 90°, which minimizes the ram drag and improves the aerodynamic efficiency.

To demonstrate this advantage, two CFJ transonic airfoils with different suction slot opening angles are tested computationally. The suction slot arrangements are shown in Figure 10.

Figure 11 presents the aerodynamic coefficients under different C_μ. As expected, the θ_2=78° case has slightly lower C_L than the θ_2=12° case, but its C_D reduction is more significant. Consequently, the θ_2=78° case achieves higher aerodynamic efficiency $(\frac{L}{D})_c$ for the same C_L, with P_c roughly the same for both cases.

Based on this finding, the suction slot opening angle θ_2=78° is employed for the trade study hereafter.

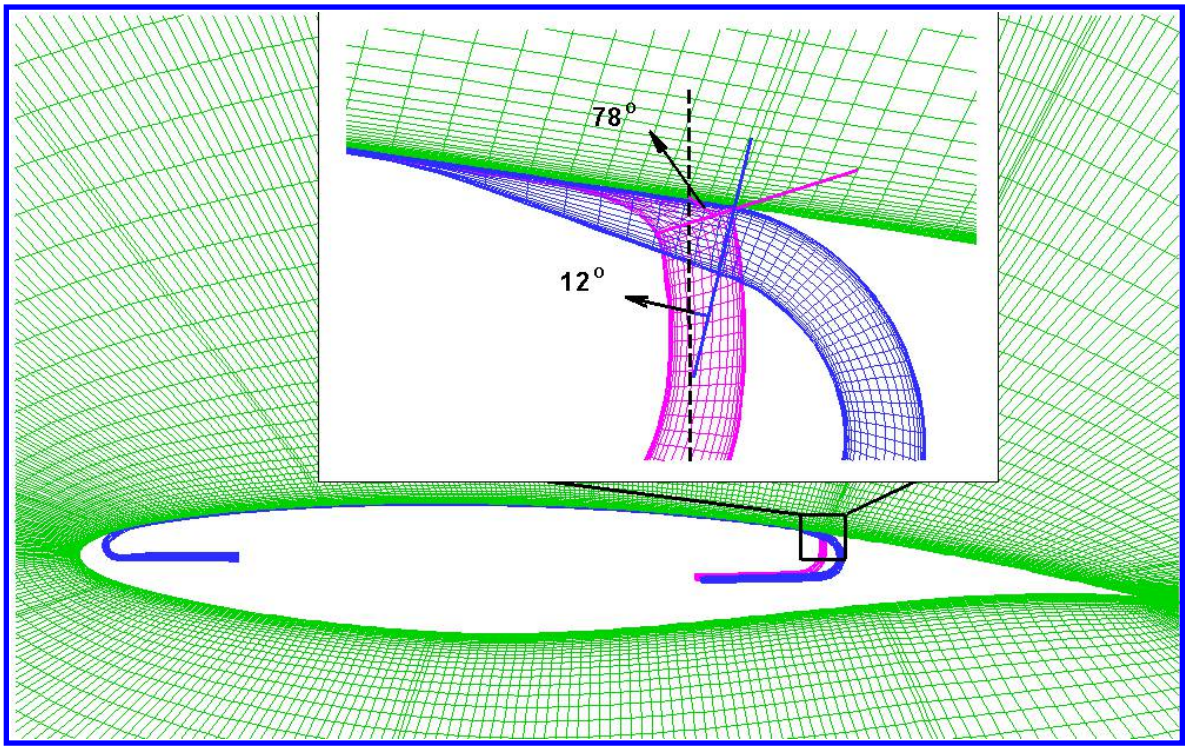

Figure 10: The CFJ transonic airfoil with different suction opening slot angle.

III.B.3. CFJ Suction Slot Width

In order to achieve higher C_μ without the suction slot being choked, the CFJ suction slot width needs to be properly sized. Three cases with suction slot width being 0.6%, 0.9% and 1.2% chord length are considered, while injection slot width is fixed at 0.6% chord length.

Figure 12 shows the CFJ transonic airfoil with the suction slot width of 0.6%, 0.9% and 1.2% chord length, respectively. Figure 13 shows the effect of suction slot width on aerodynamic performance. It is shown that for C_μ from 0 to 0.001 all the slot width cases give almost the same performance. However, as C_μ goes higher to obtain higher C_L, the 0.6% and 0.9% chord cases generate more drop in $(\frac{L}{D})_c$ due to slot being choked and leads to higher P_c increase. Thus the 1.2% chord is used to obtain higher C_L without losing aerodynamic efficiency.

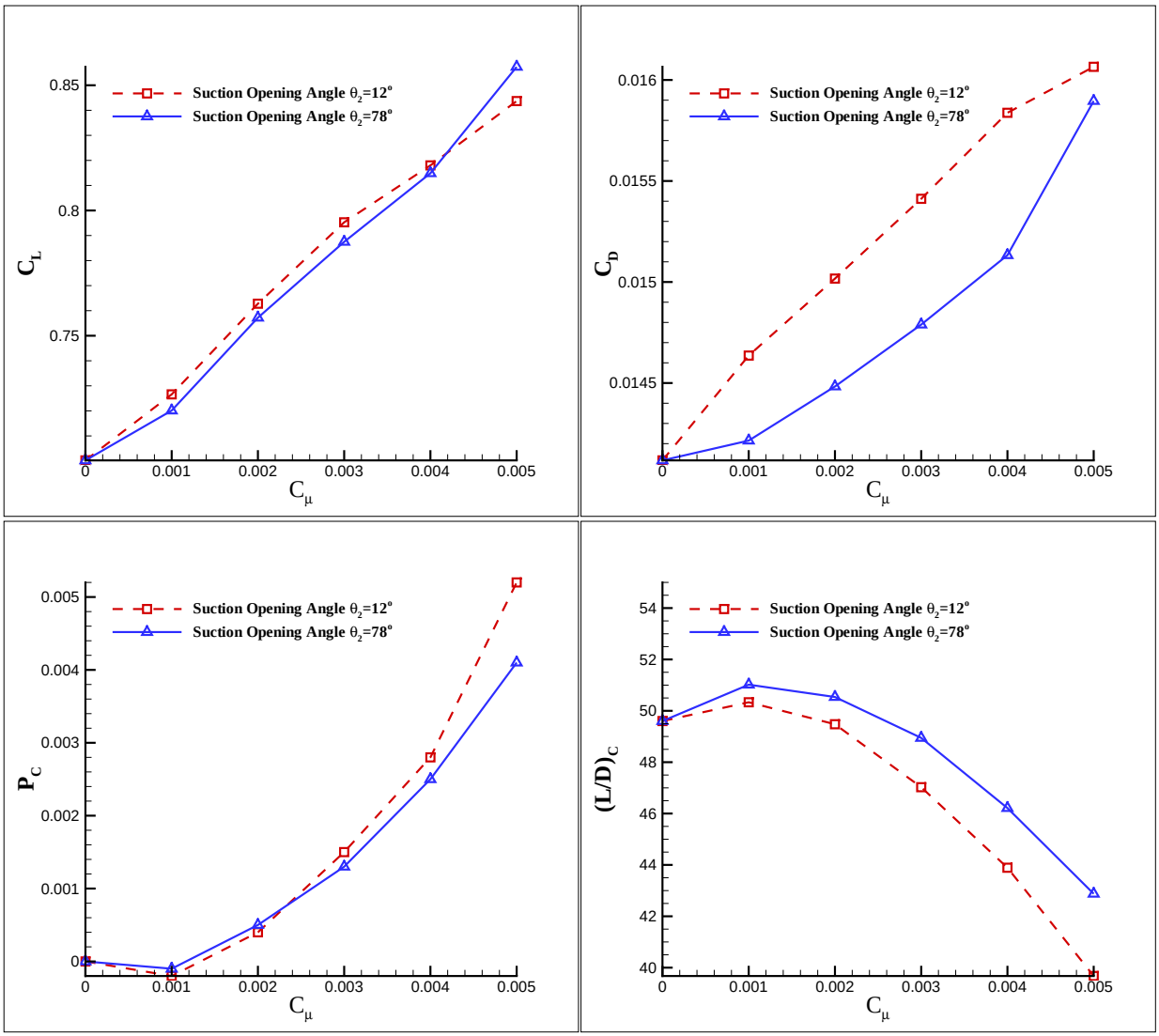

Figure 11: Aerodynamic coefficients for different CFJ suction slot opening angle θ_2 under different C_μ.

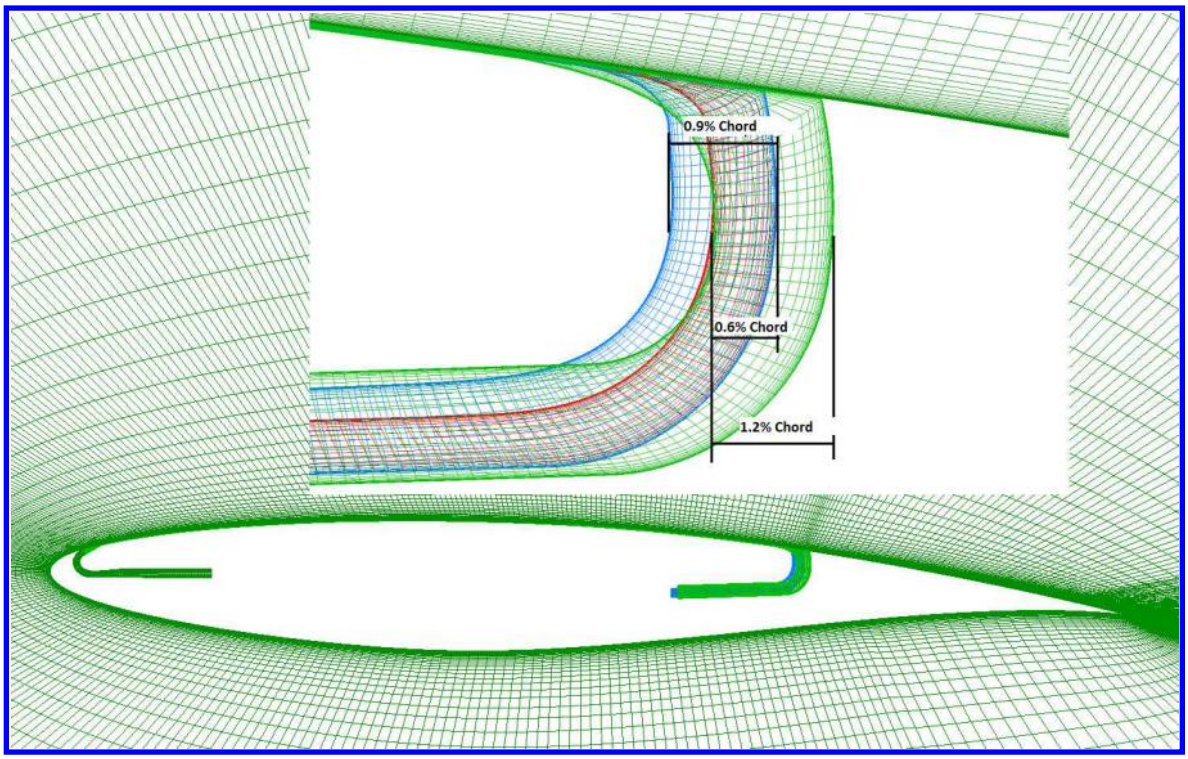

Figure 12: The CFJ transonic airfoil with different suction slot width arrangement.

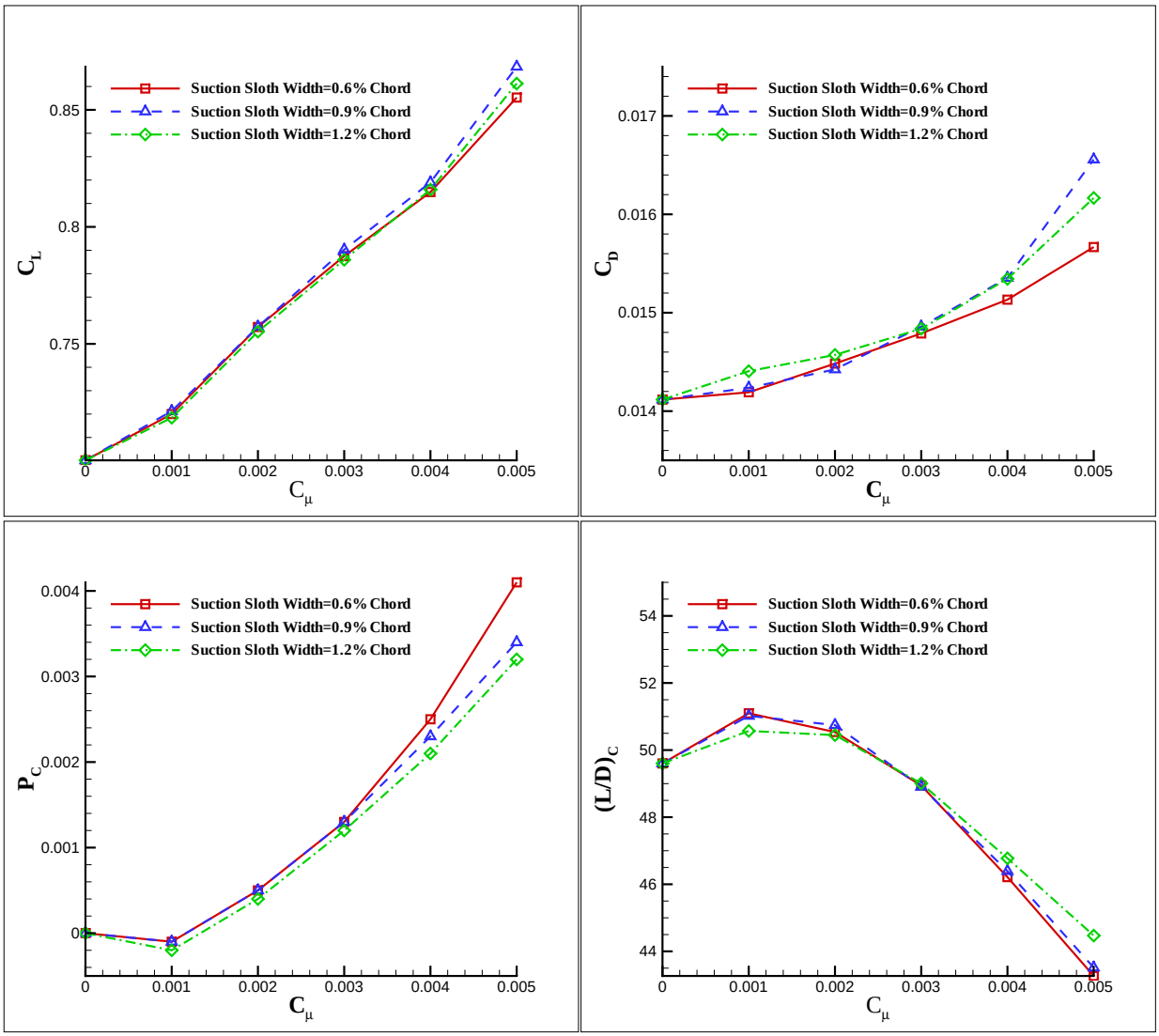

Figure 13: Aerodynamic coefficients for different CFJ suction slot width under different C_μ.

III.B.4. CFJ Suction Slot Opening Location

For a CFJ transonic airfoil, the jet has the effect to expand the supersonic region due to the induction of higher jet velocity with the terminal shock moved more downstream. The stronger the jet, the more downstream the shock will be located. When the shock wave reaches the suction slot location, the suction duct may get choked. It is hence desirable to locate the suction slot sufficiently downstream to avoid the shock reaching the slot as long as the thickness of the airfoil permits.

Figure 14 demonstrates the CFJ transonic airfoils with suction slot located at 70%, 75% and 80% chord location. The 70% case gets choked at C_μ=0.015 while both the 75% and 80% case get choked at C_μ=0.025.

Figure 15 plots the aerodynamics coefficients for each cases. At higher C_μ, the 80% suction location case gives the best C_L and $(\frac{L}{D})_c$ since there is some distance between the shock wave and the suction location.

Figure 16 presents the Mach contours at choked condition for each case. It is shown that the shock wave already reaches the suction location for 70% with the suction duct choked. The 80% case has the longest distance between the shock and the suction location. Both the 75% and 80% cases are choked at $C_\mu = 0.025$. Since the C_μ range studied is below 0.01, the 75% suction location is hence used with sufficient choking margin.

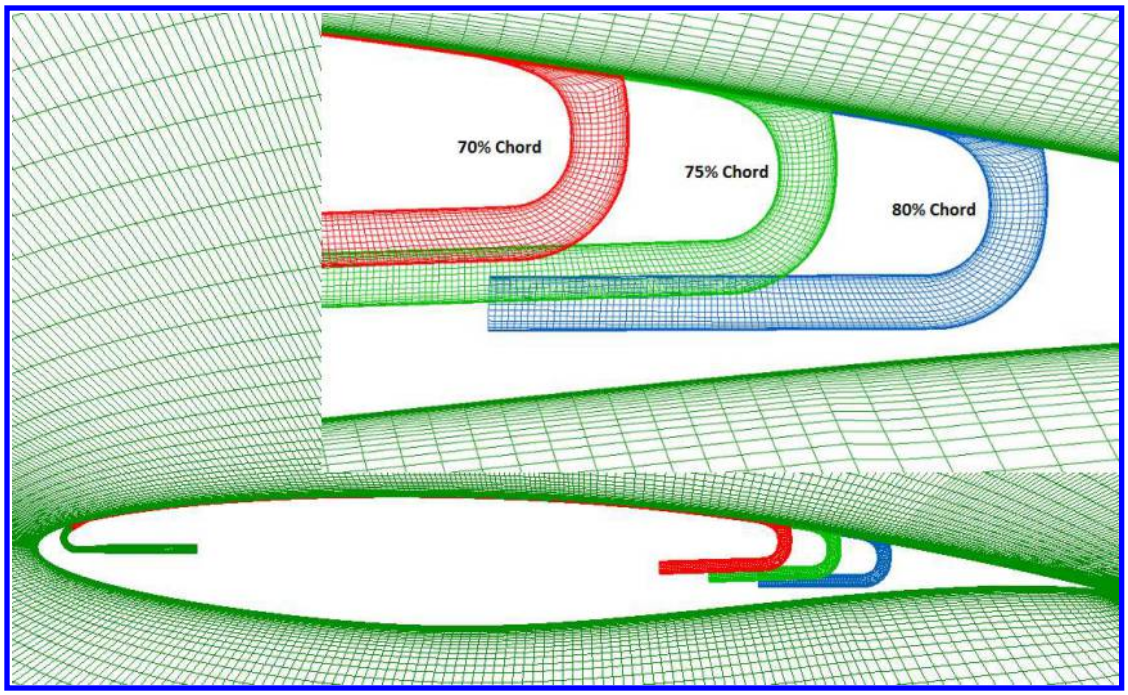

Figure 14: The CFJ transonic airfoil with different suction slot opening location.

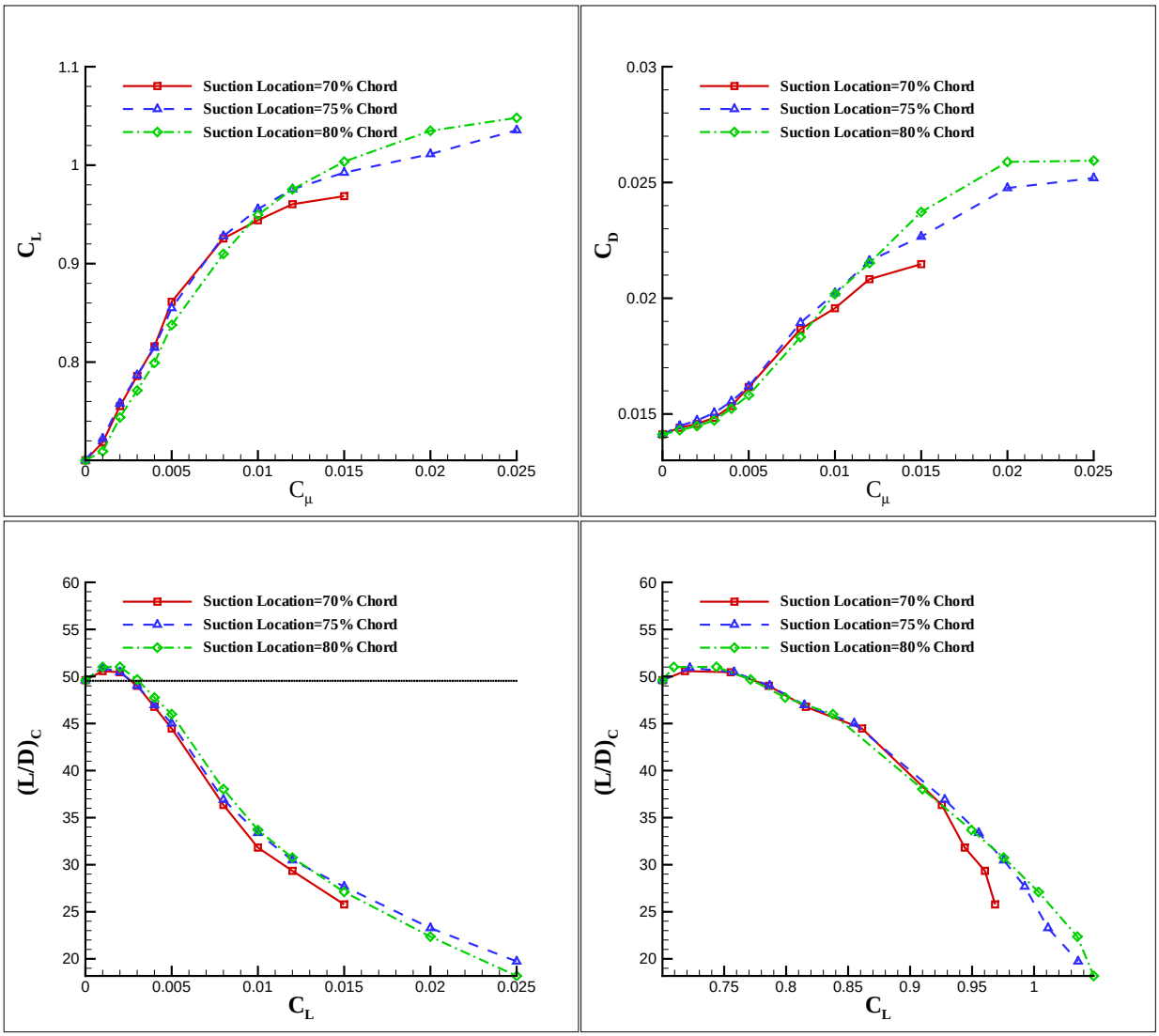

Figure 15: Aerodynamic coefficients variation with C_μ for different CFJ suction slot opening locations. (Dotted line shows the baseline $(\frac{L}{D})_c$ value.)

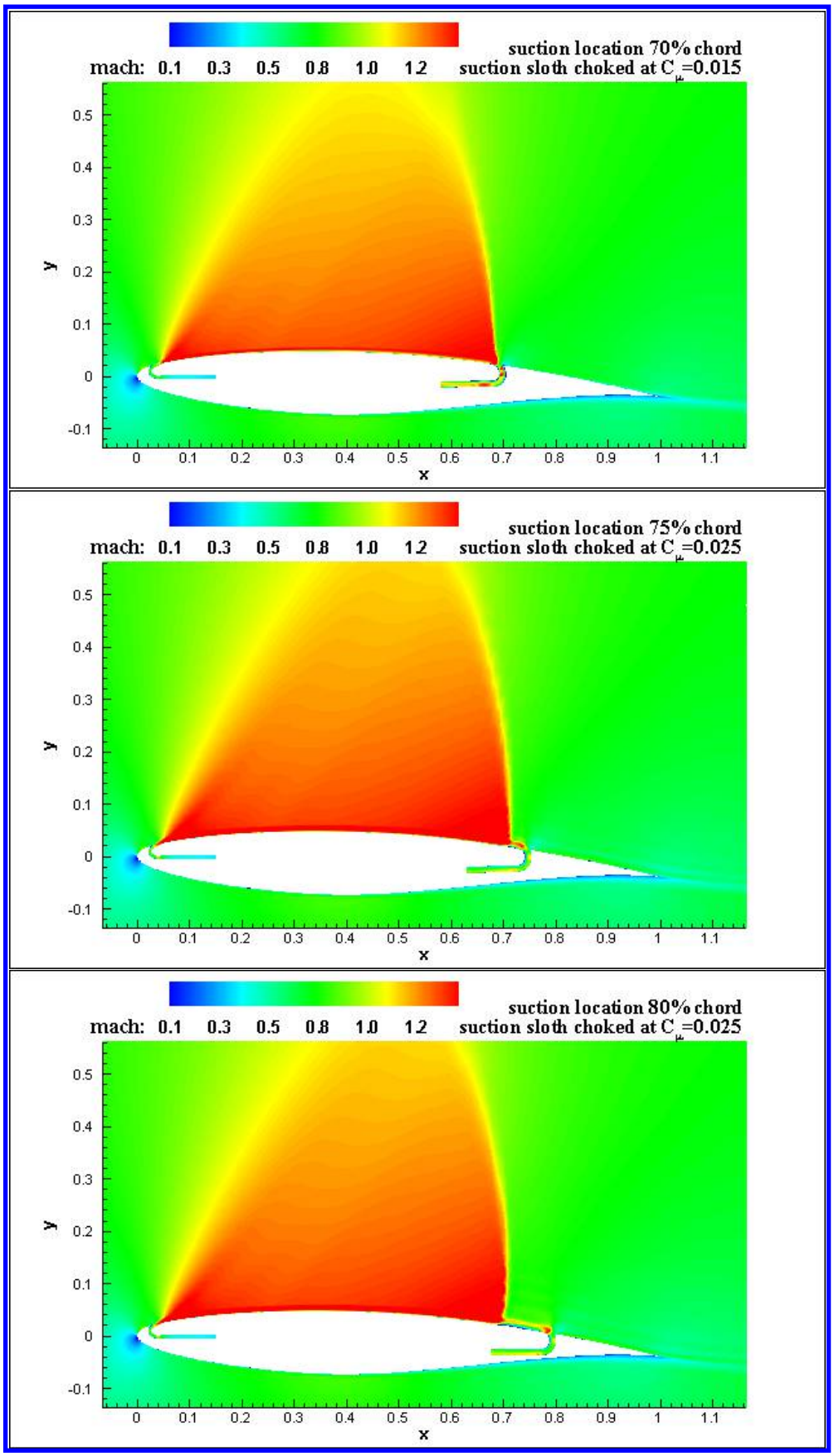

Figure 16: Mach contours for CFJ transonic airfoil with different suction slot opening location while suction slot being choked.

III.C. Aerodynamic Behavior of the CFJ Airfoil

III.C.1. Angle of Attack

The final CFJ RAE2822 airfoil configuration is determined after the trade study in section III.B. The configuration is shown in Figure 17(lower plot) and is studied for AoA varying from 0° to 5.5° with C_μ changing between 0.001 and 0.007. The CFJ pumping efficiency η of 0.9 is used for all the cases.

Figure 18(left) indicates CFJ airfoil injection velocity V_j/V_∞ versus AoA at different jet momentum coefficient C_μ. The greater the C_μ is, the greater the jet velocity becomes. However, all jet velocities are lower than the free stream velocity. Besides, all C_μ conditions show jet velocity increase linearly as AoA increases from 0° to 5.5°.

Figure 18(right) depicts the injection/suction total pressure ratio Γ versus AoA. Typically, the total pressure ratio should be greater than 1.0 to be able to drive the flow towards downstream. But because of the unique low energy expenditure configuration of CFJ, which has the injection near the suction peak of the airfoil and jet suction close to the trailing edge, the total pressure ratio between injection slot and suction slot become lower than 1.0 for $C_\mu = 0.001$ case. This means that the co-flow jet can flow by itself from the suction slot to the injection slot without using a pump. The jet flow will be driven by the high pressure near trailing edge and the low pressure near leading edge. For all the other C_μ cases, as AoA increases, the total pressure ratio first is decreased up to AoA=2°, and then start to rise to AoA=3.5°, and then is decreased again.

To further understand the trend of the total pressure ratio variation with respect to AoA, Mach number and total pressure contours at $C_\mu = 0.007$ under different AoA are plotted in Figure 19. It is shown that the total pressure at the injection slot gradually decreases as the AoA goes up from 1° to 4.5°. This is because as the AoA increases, the suction peak translates closer to the injection slot and creates a lower static pressure, and therefore requires lower total pressure to generate the same C_μ.

As the AoA increases from 1° to 2°, the suction flow condition changes slightly due to the shock location maintaining upstream enough and not being able to affect the suction flow condition too much, which explains the slight total pressure ratio Γ drop. As the AoA further increases from 2° to 3.5°, the shock wave shifts to the suction slot location, which creates a significantly high total pressure loss from 1.26 to 0.95. Therefore, Γ increases drastically as AoA increases from 2° to 3.5°.

When the AoA goes up beyond 3.5°, flow separation occurs around the suction slot region and the shock wave shifts upstream due to the boundary layer separation. The shock wave interacting the boundary layer is oblique instead of a normal shock. It creates expansion waves immediately downstream of the shock wave. Even though it generates flow separation, the total pressure loss is less due to the weaker oblique shock interacting with the boundary layer. Thus, Γ decreases as the AoA increases from 3.5° to 5.5°.

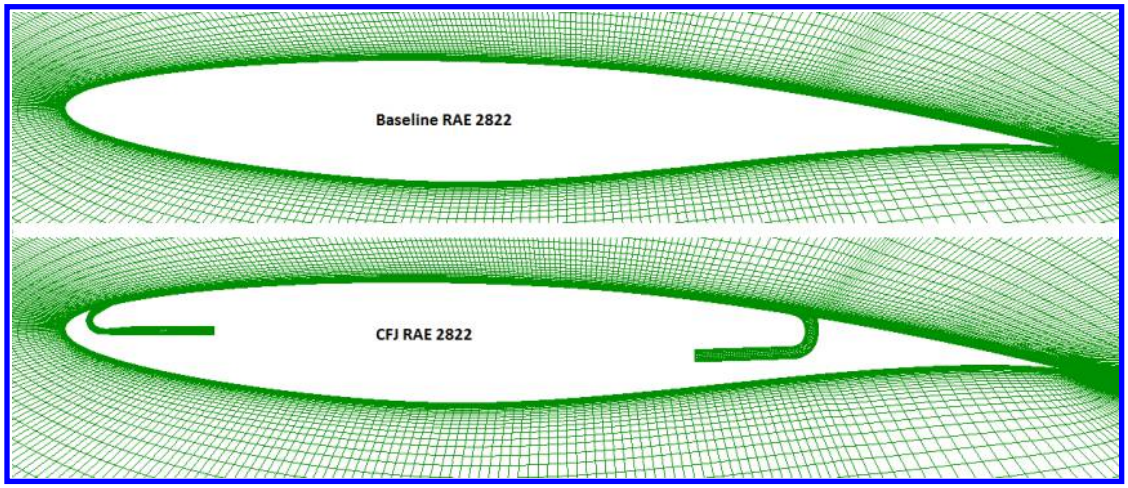

Figure 17: The CFJ RAE2822 airfoil and the baseline RAE2822 airfoil.

Figure 20 demonstrates the aerodynamic coefficients variation with respect to AoA for both the baseline and CFJ airfoil. There are several observations: First, the CFJ airfoil exhibits higher C_L for all AoA and the C_L augmentation is increased as C_μ increases. Second, for the AoA smaller than 2.2°, the CFJ airfoil generates lower drag than the baseline. It is because the CFJ produces thrust while maintaining a weak shock wave. Third, CFJ is beneficial to both $(\frac{L}{D})$ and $(\frac{L}{D})_C$ when AoA is smaller than 2.5°. For higher AoA,

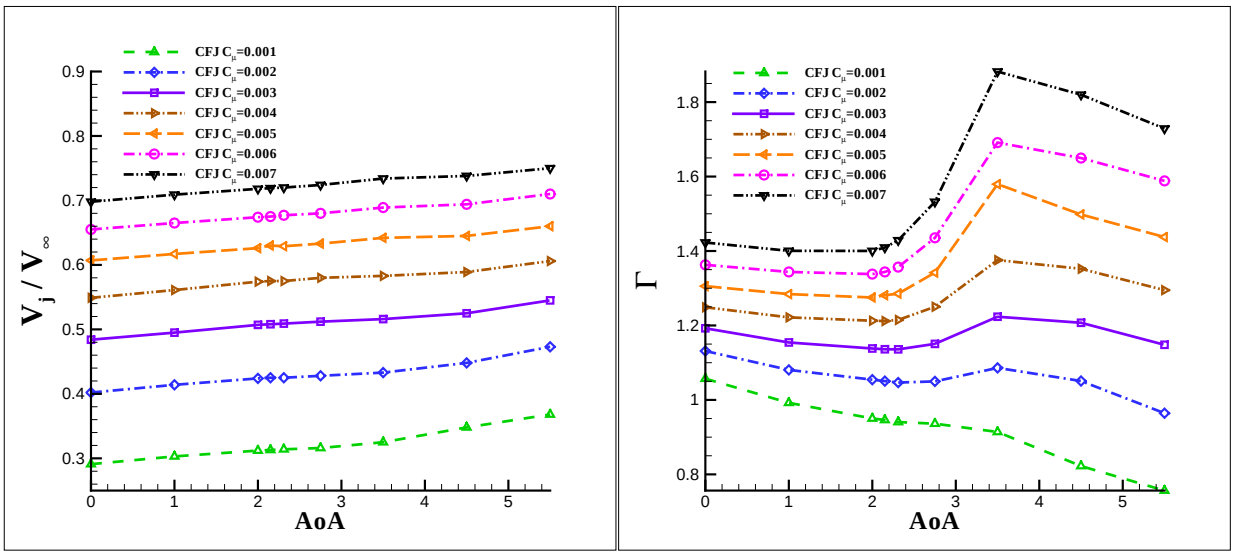

Figure 18: CFJ airfoil injection velocity(left) and injection/suction total pressure ratio(right) versus angle of attack for different jet moment coefficient.

$(\frac{L}{D})$ and $(\frac{L}{D})_C$ decrease due to stronger shock wave. Fourth, the nose-down pitching moment coefficient C_M of CFJ airfoil is higher than that of the baseline airfoil. This may require a larger control surface to trim the aircraft.

Figure 21 shows the drag polar of the CFJ airfoil compared with the baseline airfoil with the AoA varying from 0° to 5.5°. It indicates that CFJ airfoil significantly increase the lift coefficient compared with baseline airfoil with the same drag coefficient for all C_μ conditions. The maximum lift coefficient is increased by about 25.6% from from 0.926 to 1.163. For the same lift coefficient, the CFJ airfoil has much less drag. The drag reduction is because the CFJ energizes the boundary layer and the wake velocity deficit is less than the baseline airfoil without CFJ.[12–15,36] The reduced aerodynamic drag hence enables using a smaller engine. The drag reduction is at the cost of the CFJ pumping power. For a complete measurement of aerodynamic efficiency, the power consumption of the CFJ should be included as a part of equivalent drag as defined in equation (13). We call it as corrected drag coefficient $C_D + P_C$.

Figure 22 is the lift coefficient against the corrected drag coefficient $C_D + P_C$. What is very encouraging is that there is a significant efficiency gain when the lift coefficient is greater than 0.65. The higher the lift coefficient is, the more the efficiency improvement gets. For example, for $C_L = 0.85$ at $C_\mu = 0.007$, the corrected drag coefficient is 0.019, lower than that of the baseline drag coefficient of 0.025. It brings a net aerodynamic efficiency $(\frac{L}{D})_c$ gain of 32%. Furthermore, the CFJ airfoil can fly at C_L of 1.15, far greater than the maximum lift coefficient of 0.92 for the baseline airfoil.

Figure 23 plots the results of $(\frac{L}{D})$ verses C_L. Several characteristic points are selected for comparison between the baseline airfoil and CFJ airfoil. Point 1 is the peak $(\frac{L}{D})$ point of the CFJ airfoil. Point 1b is the peak $(\frac{L}{D})$ point of the baseline airfoil. Point 2 is the maximum C_L point of the CFJ airfoil. Point 2b is the maximum C_L point of the baseline airfoil. Point 3 is the point of the CFJ airfoil with nearly the same C_L as Point 1b. Table 3 gives the quantitative comparison of all the characteristic points in Figure 23. It shows a drastic $(\frac{L}{D})$ improvement due to CFJ implementation.

Figure 24 depicts the results of $(\frac{L}{D})_c$ verses C_L. A few characteristic points are also selected for comparison purpose. Point 1b and Point 2b are selected the same way as defined in Figure 23. Point 1c is the peak efficiency $(\frac{L}{D})_c$ point of the CFJ airfoil. Point 2c is the maximum C_L point of the CFJ airfoil. Point 3c is the point of the CFJ airfoil that has the same efficiency $(\frac{L}{D})_c$ as Point 1b. Table 4 compares those points for the corrected aerodynamic efficiency $(\frac{L}{D})_c$ with a few observations: 1) Comparing the maximum aerodynamic efficiency point 1c and 1b between the CFJ and baseline airfoil, the CFJ airfoil has the $(\frac{L}{D})_c$ improved by 14.5% from 49.68 to 56.86 with the C_L improved by 18.7% at the same time from 0.611 to 0.725; 2) Comparing point 2b and point 2c, the maximum lift coefficient is improved by 25.6% from 0.926 to 1.163, whereas the $(\frac{L}{D})_c$ drops slightly from 21.27 to 19.58; 3) Comparing point 3c and point 1b, the C_L is improved by 30.1% with the $(\frac{L}{D})_c$ increased by 2.7% simultaneously.

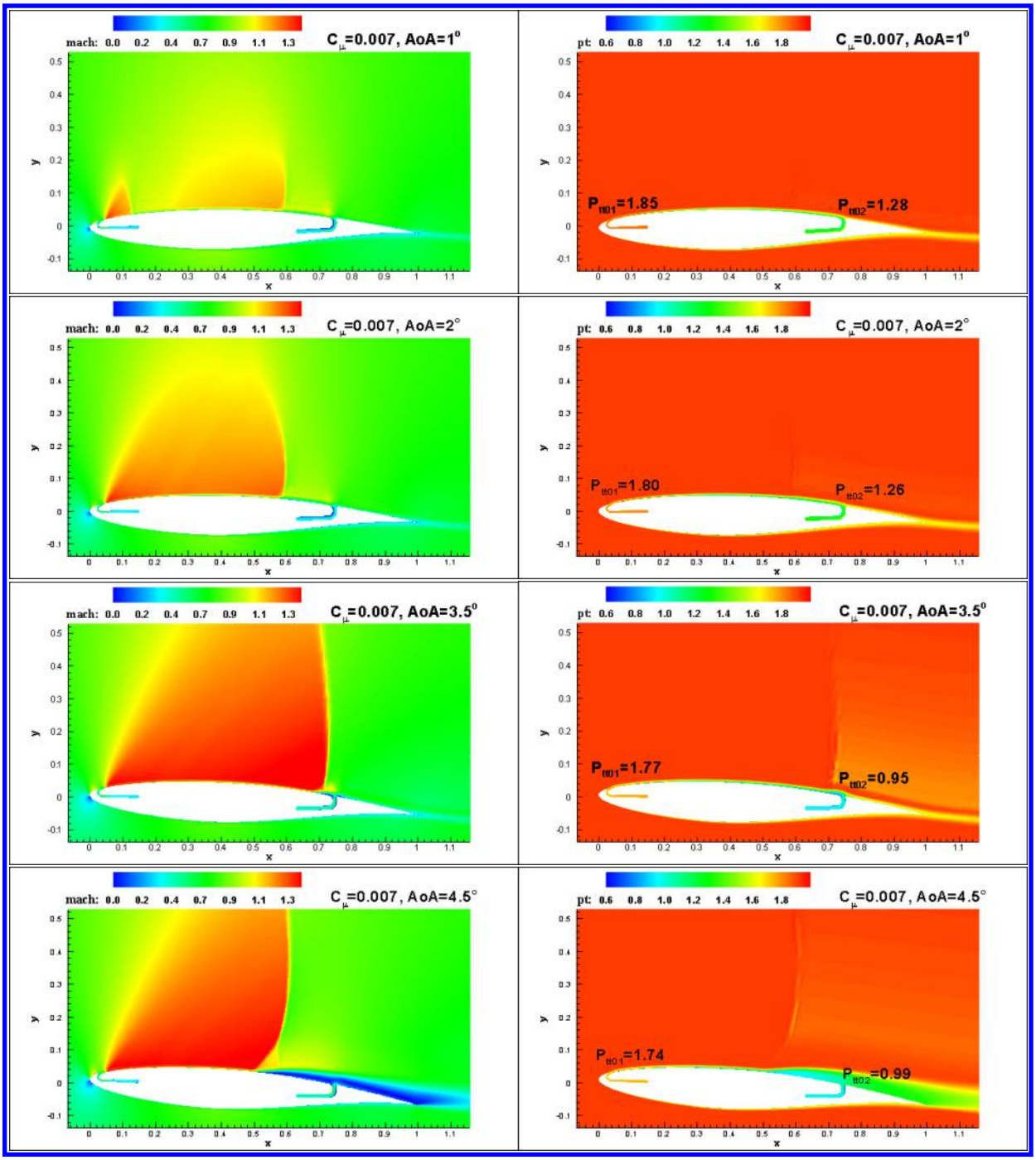

Figure 19: Mach number(left) and total pressure(right) contours at $C_\mu = 0.007$ under different angle of attack.

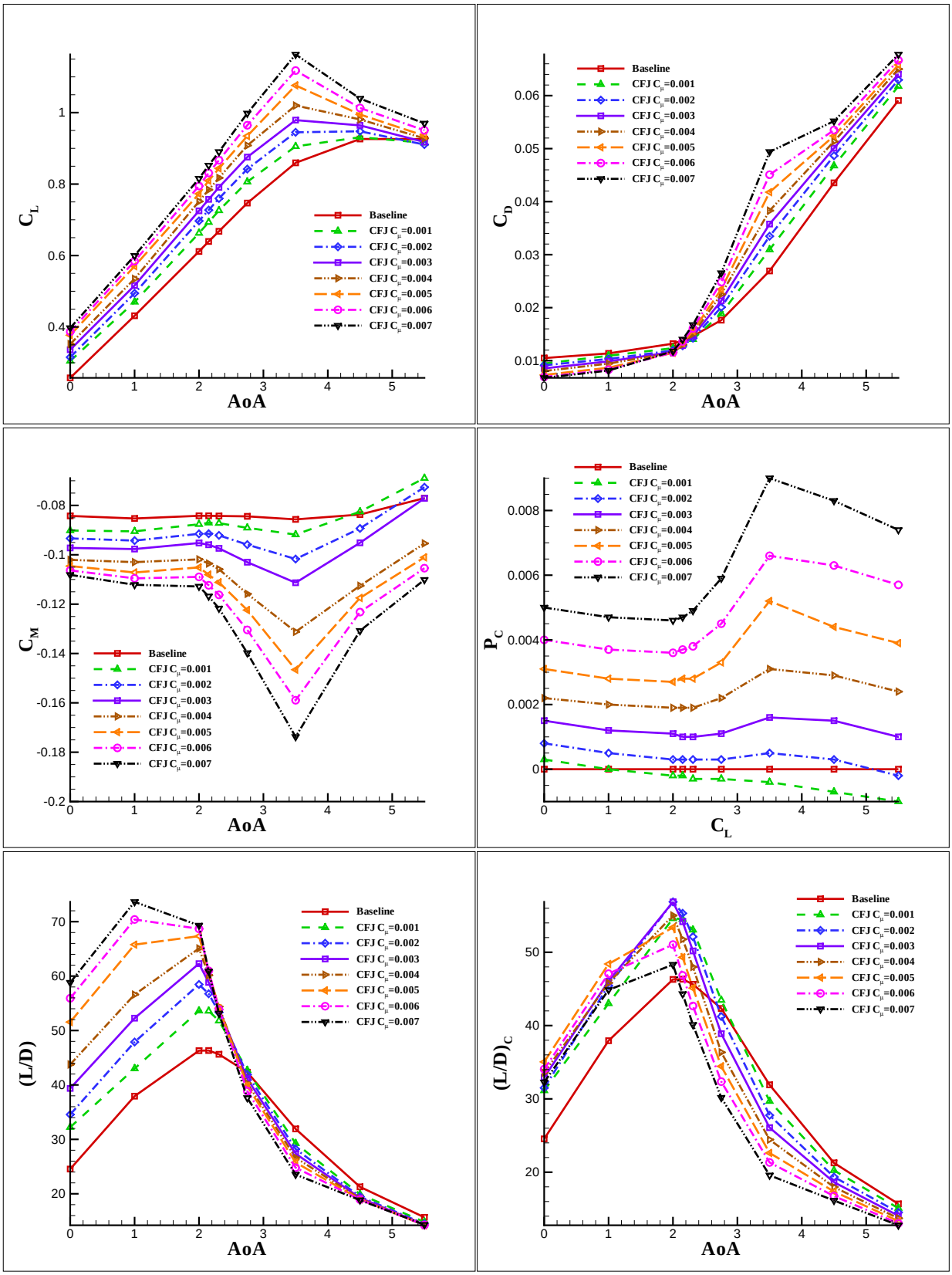

Figure 20: Aerodynamic coefficients of the CFJ airfoil and the baseline airfoil for angle of attack changing from 0° to 5.5°.

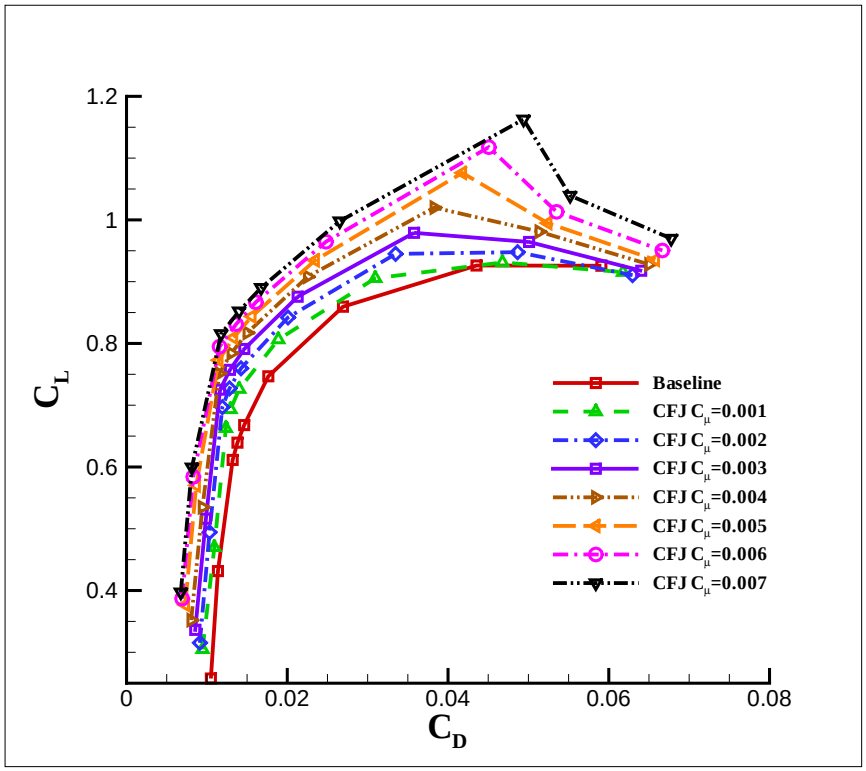

Figure 21: The drag polar curves of the CFJ airfoil and the baseline airfoil for angle of attack changing from 0° to 5.5°.

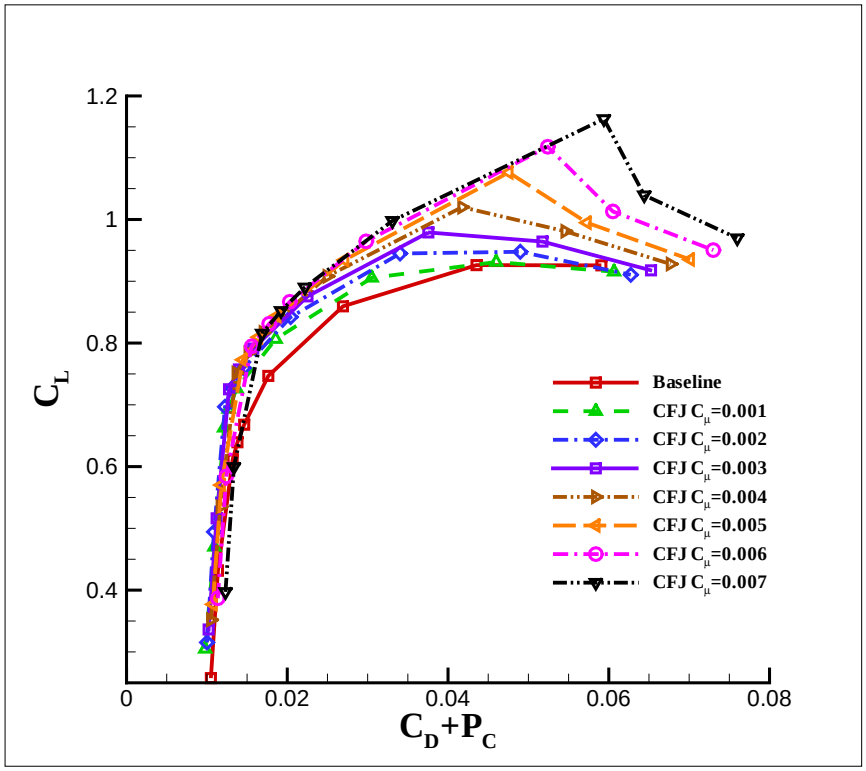

Figure 22: The corrected drag polar curves of the CFJ airfoil and the baseline airfoil for angle of attack changing from 0° to 5.5°.

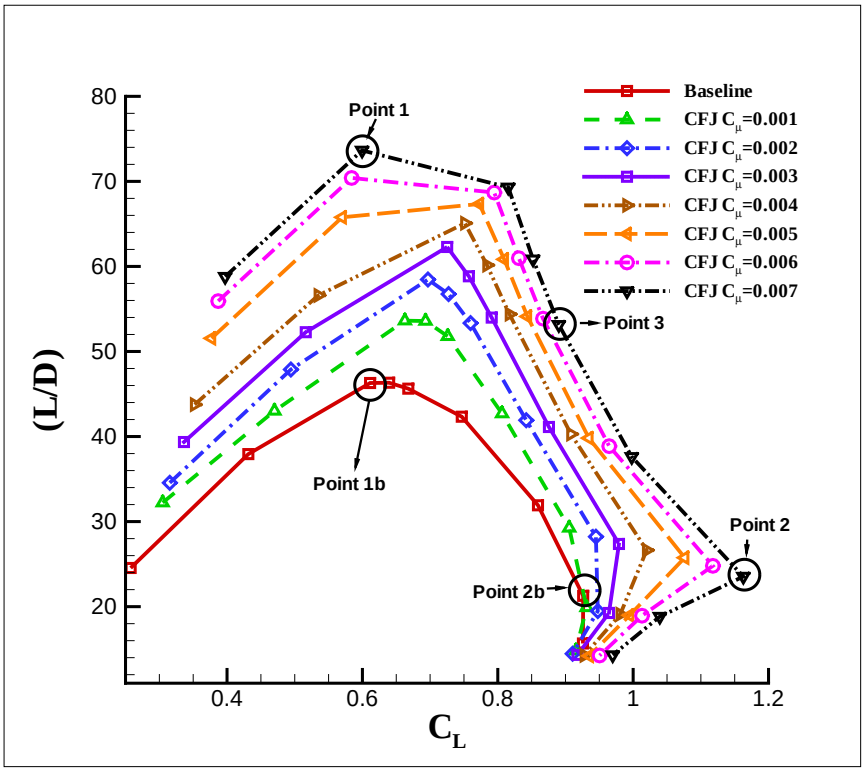

Figure 23: The aerodynamic performance curves of the CFJ airfoil and the baseline airfoil for angle of attack changing from 0° to 5.5°.

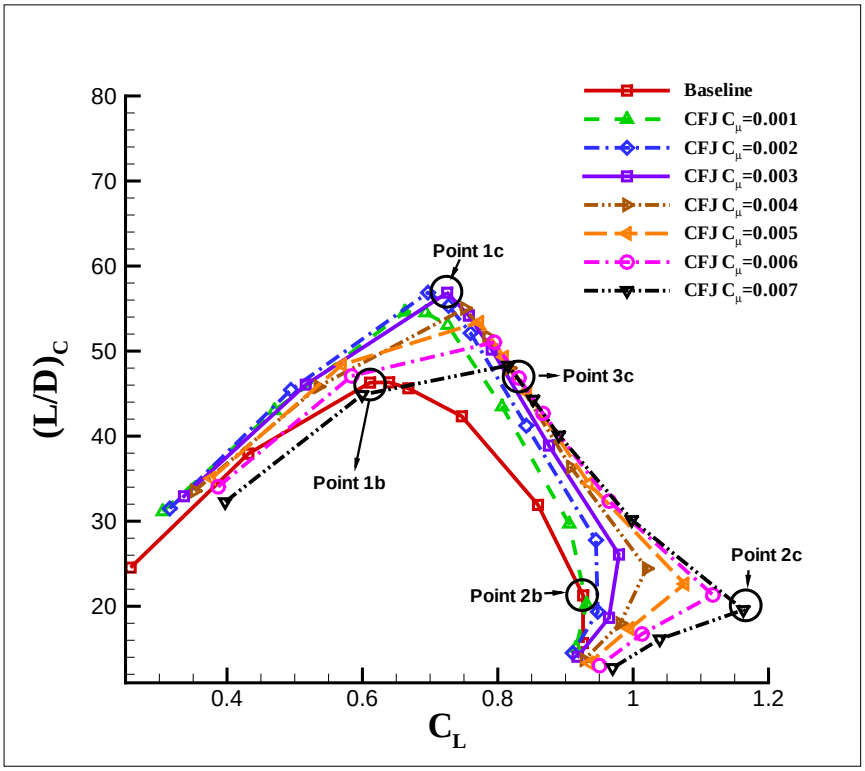

Figure 24: The corrected aerodynamic performance curves of the CFJ airfoil and the baseline airfoil for angle of attack changing from 0° to 5.5°.

Table 3: Aerodynamics coefficients comparison between the CFJ airfoil and the baseline airfoil. (Referring to Figure 23 for each point.)

	Point 1	Point 1b	Improvement
α	1.0°	2.0°	N/A
C_L	0.600	0.611	-1.8%
$(\frac{L}{D})$	73.64	49.68	48.2%
	Point 3	Point 1b	Improvement
α	2.31°	2.0°	N/A
C_L	0.890	0.611	45.7%
$(\frac{L}{D})$	53.14	49.68	7.0%
	Point 2	Point 2b	Improvement
α	3.5°	4.5°	N/A
C_L	1.163	0.926	25.6%
$(\frac{L}{D})$	23.54	21.27	10.7%

Table 4: Corrected aerodynamics coefficients comparison between the CFJ airfoil and the baseline airfoil. (Referring to Figure 24 for each point.)

	Point 1c	Point 1b	Improvement
α	2.0°	2.0°	N/A
C_L	0.725	0.611	18.7%
$(\frac{L}{D})_c$	56.86	49.68	14.5%
	Point 3c	Point 1b	Improvement
α	2.0°	2.0°	N/A
C_L	0.795	0.611	30.1%
$(\frac{L}{D})_c$	51.04	49.68	2.7%
	Point 2c	Point 2b	Improvement
α	3.5°	4.5°	N/A
C_L	1.163	0.926	25.6%
$(\frac{L}{D})_c$	19.58	21.27	-7.9%

III.C.2. Detailed Flow Field Comparison

Figure 25 compares the Mach contours, surface pressure and isentropic Mach number distributions for the peak efficiency points of the baseline and the CFJ airfoil with $C_\mu = 0.003$. The Mach contours show that the CFJ airfoil expands the supersonic region to a larger area with overall higher Mach number. As displayed in the surface isentropic Mach number distributions, the CFJ airfoil has a higher peak suction Mach number near the leading edge enhanced by the induction effect of the CFJ injection. The supersonic flow Mach number is then attenuated by the compression waves reflected from the sonic boundary and airfoil surface as described by Harris.[5] The normal shock of the CFJ airfoil is pushed further downstream than that of the baseline airfoil. The higher leading edge Mach number and more downstream shock location all provide the CFJ airfoil with higher lift coefficient. The Mach number right after the shock of the CFJ airfoil is closer to 1 than the baseline airfoil, which is more desirable to reduce the entropy increase as pointed out by Harris.[5]

More Mach contours zoom-in comparisons between the baseline airfoil and the CFJ airfoil at the peak efficiency condition are further carried out. Mach number contours around the shock region are depicted in Figure 26. It can be seen that the CFJ airfoil has thicker high momentum layer near the wall compared to the baseline airfoil. The boundary layer thickness of the CFJ airfoil tends to be thicker after the shock due to the stronger shock-wave/boundary-layer interaction. The Mach contours in the trailing edge wake region as shown in Figure 27 clearly indicate a smaller low Mach number region in the CFJ airfoil case.

Figure 28 compares the Mach contours, surface pressure and isentropic Mach number distributions for the maximum lift coefficient points of the baseline and the CFJ airfoil(point 2b and point 2 in Figure 23) with $C_\mu = 0.007$. Both the Mach contours and surface distributions clearly show that the shock wave of the CFJ airfoil occurs much more downstream than the baseline airfoil. This effect of the CFJ airfoil enormously increases the lift coefficient. Besides, the contours also show that the CFJ airfoil generates much less low momentum wake region than the baseline.

Figure 29 compares the baseline peak efficiency point with the CFJ airfoil point that exhibits the same efficiency but higher lift(point 1b and 3c in Figure 24) with $C_\mu = 0.006$. As shown in the contours, the CFJ airfoil not only induces the shock wave to occur more towards trailing edge, but also uniformly increases the velocity of the supersonic region, while maintaining the majority of Mach number below 1.3 and generating smaller low momentum wake region. All these factors of the CFJ airfoil contribute to greater circulation around the airfoil at low expenditure, and eventually the capability of yielding much higher lift coefficient while maintaining the same aerodynamic efficiency.

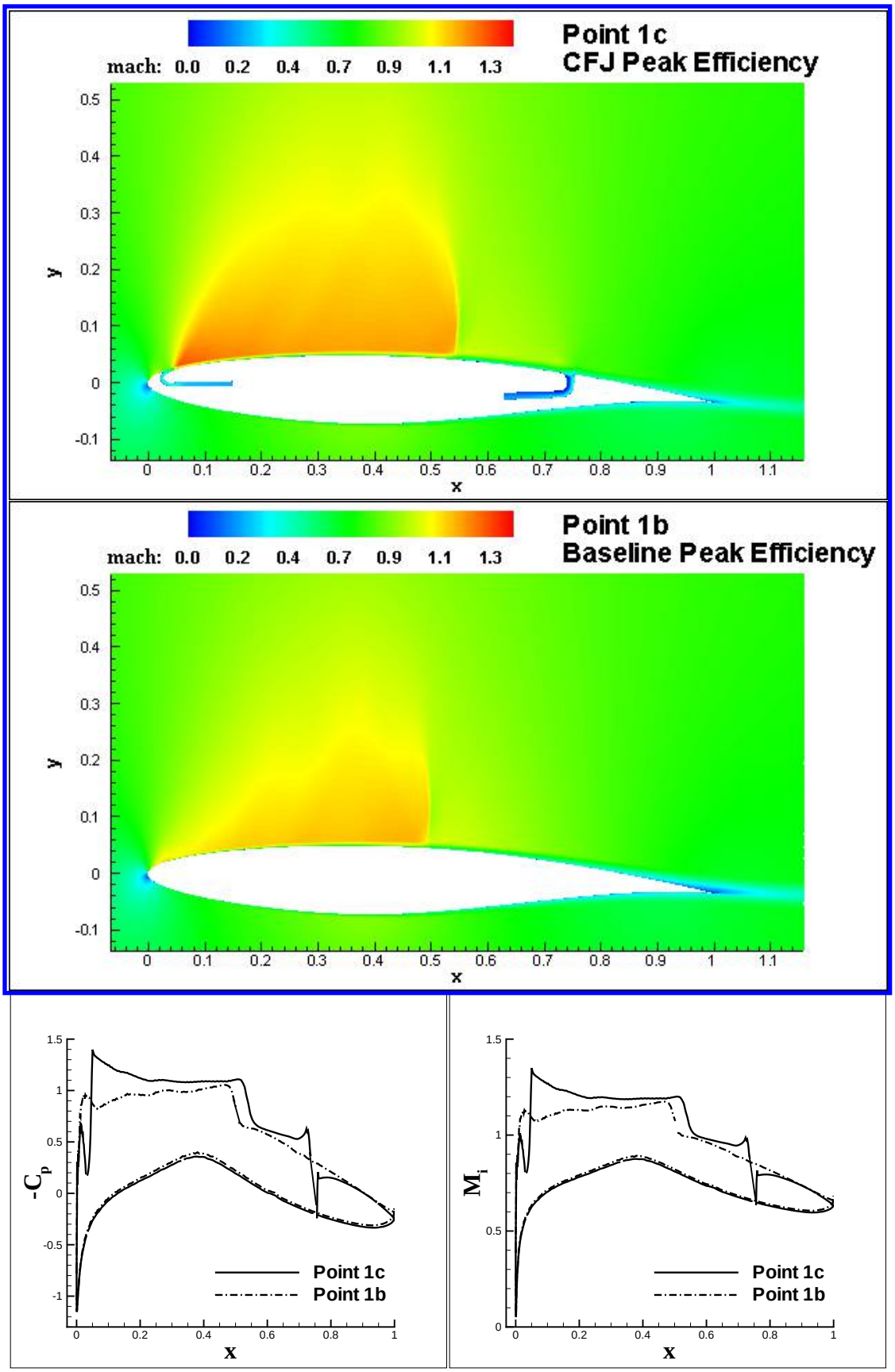

Figure 25: Mach contours, surface pressure distribution and isentropic Mach distribution comparison between the CFJ airfoil(point 1c) and the baseline airfoil(point 1b) at the peak efficiency condition with $C_\mu = 0.003$.

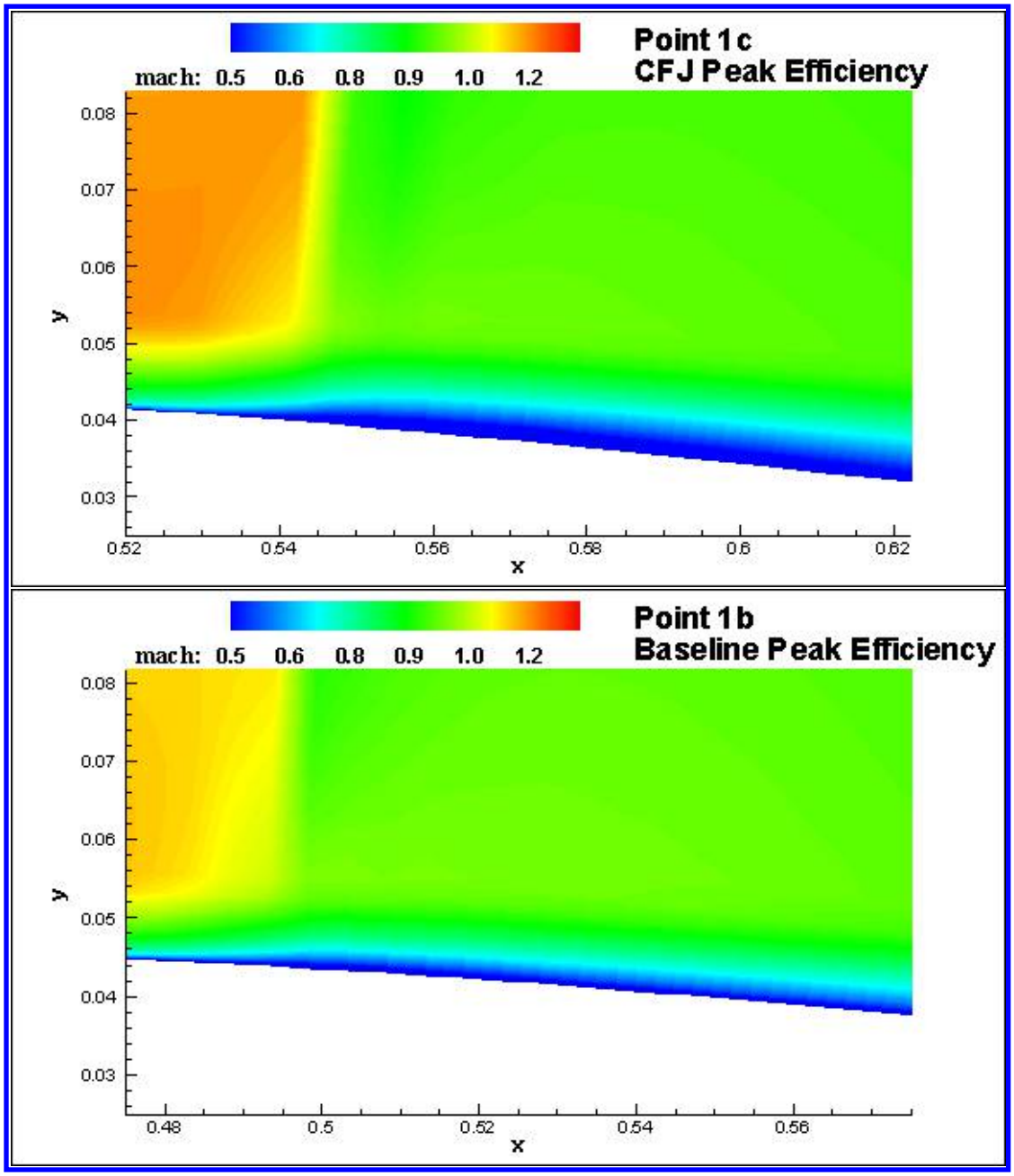

Figure 26: Near wall and after shock region Mach contour comparison between the CFJ airfoil(point 1c) and the baseline airfoil(point 1b) at the peak efficiency condition with $C_\mu = 0.003$.

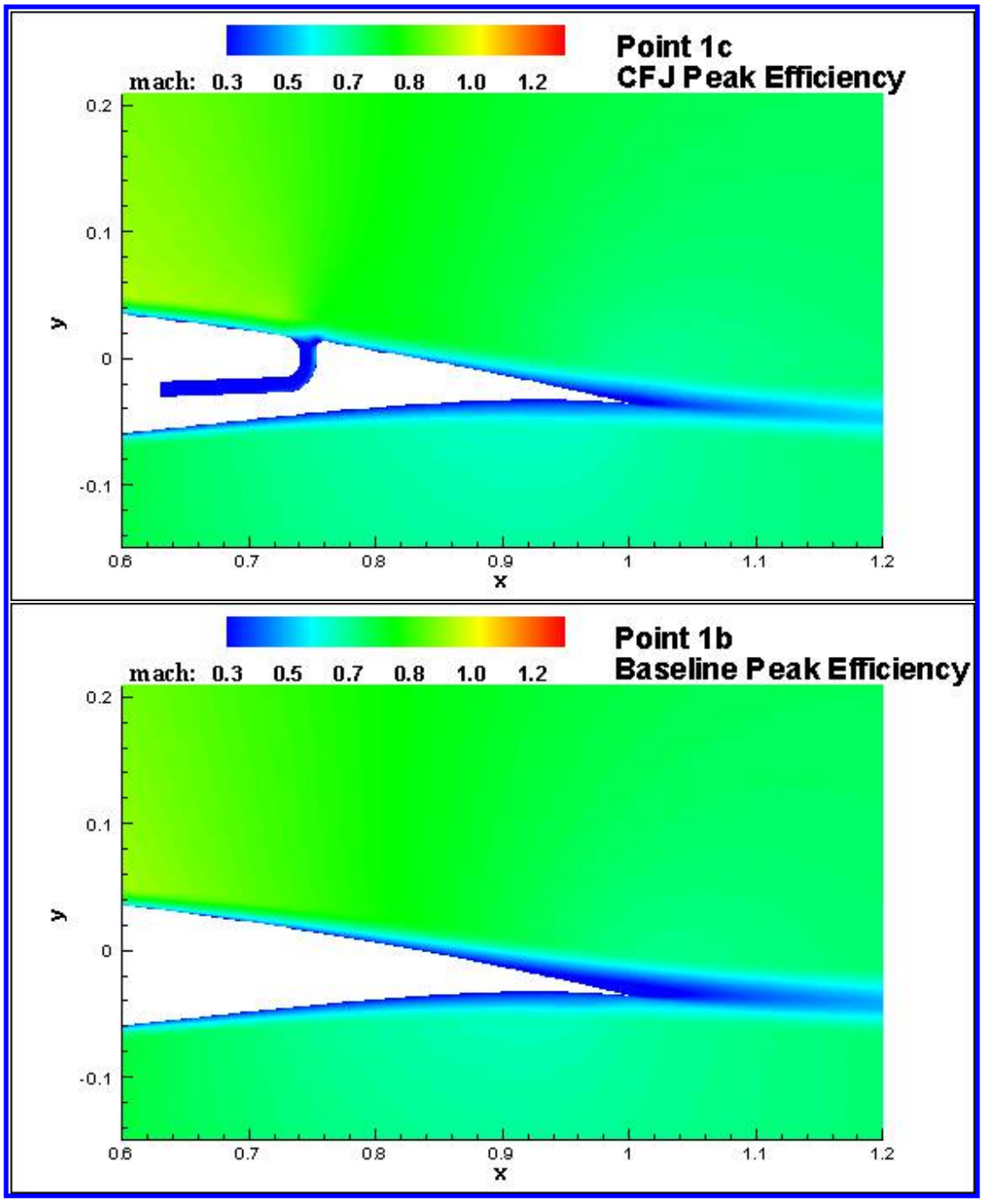

Figure 27: Wake comparison between the CFJ airfoil(point 1c) and the baseline airfoil(point 1b) at the peak efficiency condition, $C_\mu = 0.003$.

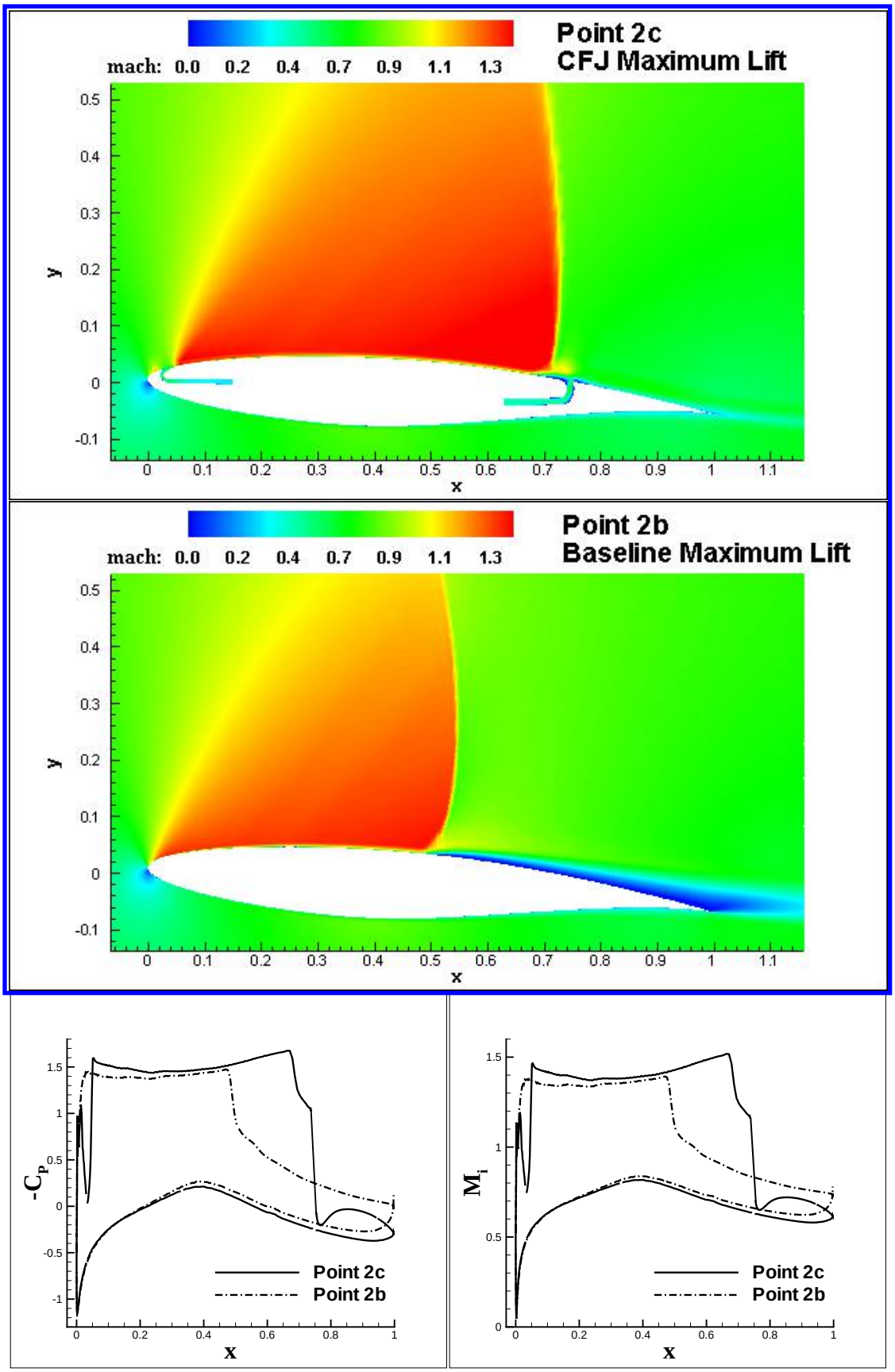

Figure 28: Mach contours, surface pressure distribution and isentropic Mach distribution comparison between the CFJ airfoil(point 2c) and the baseline airfoil(point 2b) at maximum lift condition, $C_\mu = 0.007$.

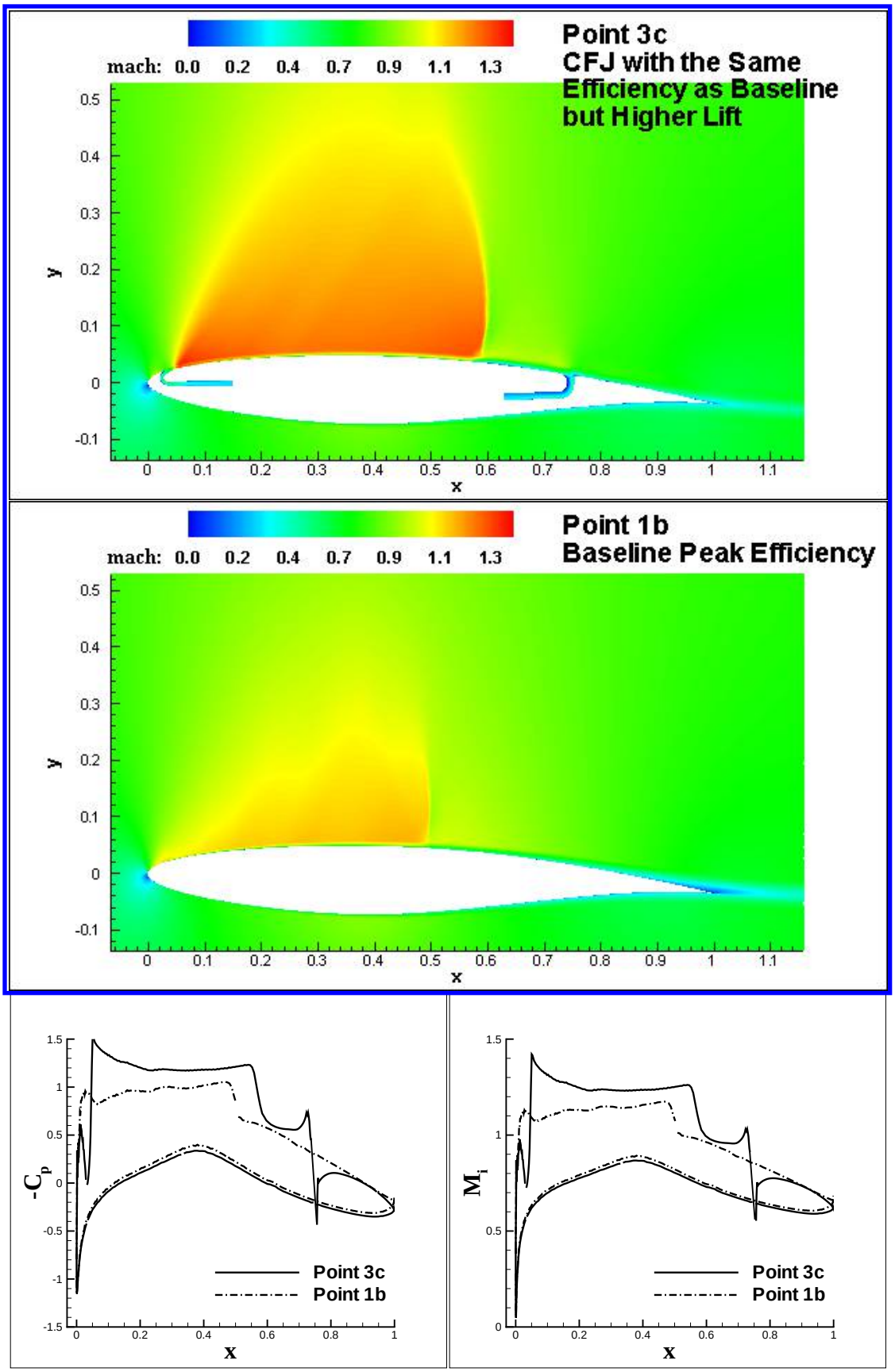

Figure 29: Mach contours, surface pressure distribution and isentropic Mach distribution comparison between between the CFJ airfoil(point 3c) and the baseline airfoil(point 1b).

III.C.3. Shock and Wake Region Analysis

To investigate the effect of the CFJ on the normal shock wave strength, the Roe scheme[24] and the E-CUSP scheme[23] are employed to compare the shock wave strength on the suction surface of both baseline and CFJ airfoil at the peak efficiency point. To exhibit the shock wave structure, local entropy increase near the shock region has been calculated as below

$$\Delta S = C_p \ln(\frac{T_0}{T_{0\infty}}) - R \ln(\frac{P_0}{P_{0\infty}}) \tag{14}$$

where $T_{0\infty}$ and $P_{0\infty}$ correspond to the free stream total temperature and total pressure, respectively.

As shown in Figure 30, when the 451×101 mesh is employed, the E-CUSP scheme gives more concentrated shock entropy increase structure, while the Roe scheme exhibits a bifurcation near the wall with lower entropy increase. For the baseline airfoil peak efficiency point, both the schemes obtain the similar entropy strength, which appears to be thicker than that of the CFJ airfoil. For the refined mesh of 641x151 in Figure 31, both schemes capture the shock entropy contours, which is similar to the one captured by the E-CUSP scheme in the coarse mesh. Thus, the E-CUSP scheme with 641×151 mesh is employed for the following studies.

Figure 32 presents the entropy increase distributions of both the baseline and the CFJ airfoil at peak efficiency point. The distance of 5% and 15% chord length vertically above the suction surface near the shock region are chosen to plot the distributions. The results suggest CFJ has slightly higher shock entropy increase due to the higher peak Mach number before the shock.

Figure 33 shows the wake x-component velocity distributions at one chord length downstream for both baseline and CFJ airfoil peak efficiency point. Apparently, the CFJ airfoil generates smaller velocity deficit consistent with the Mach contours in Figure 27.

Figure 34 show the Mach number contours of all the aforementioned characteristics points. For Point 1b, Point 1c and Point 3c, as the C_μ increases from 0.0 to 0.006 with AoA of 2°, the normal shock location moves downstream while the high entropy increase region in the wake shrinks. For point 2b and point 2c at the maximum C_L conditions, the CFJ airfoil(point 2c) has much smaller high entropy increase(above 0.18) region due to no boundary layer separation and has the shock wave pushed further downstream.

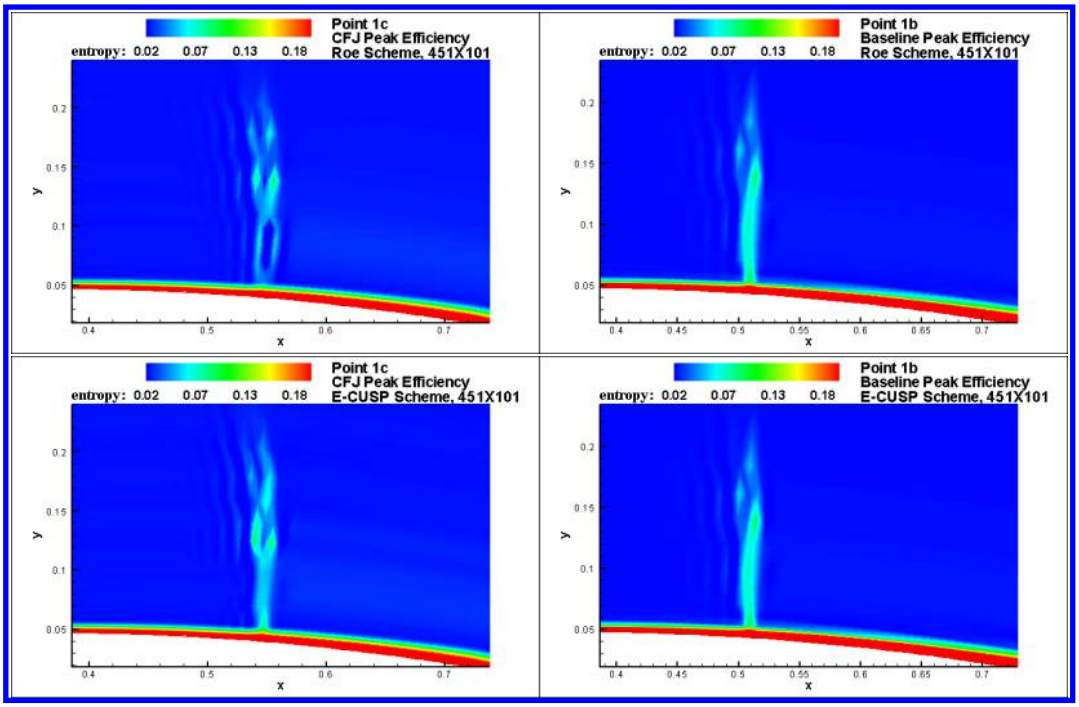

Figure 30: Shock entropy increase captured using Roe scheme and the E-CUSP scheme for the CFJ airfoil(point 1c) and the baseline airfoil(point 1b) at the peak efficiency condition using 451×101 mesh.

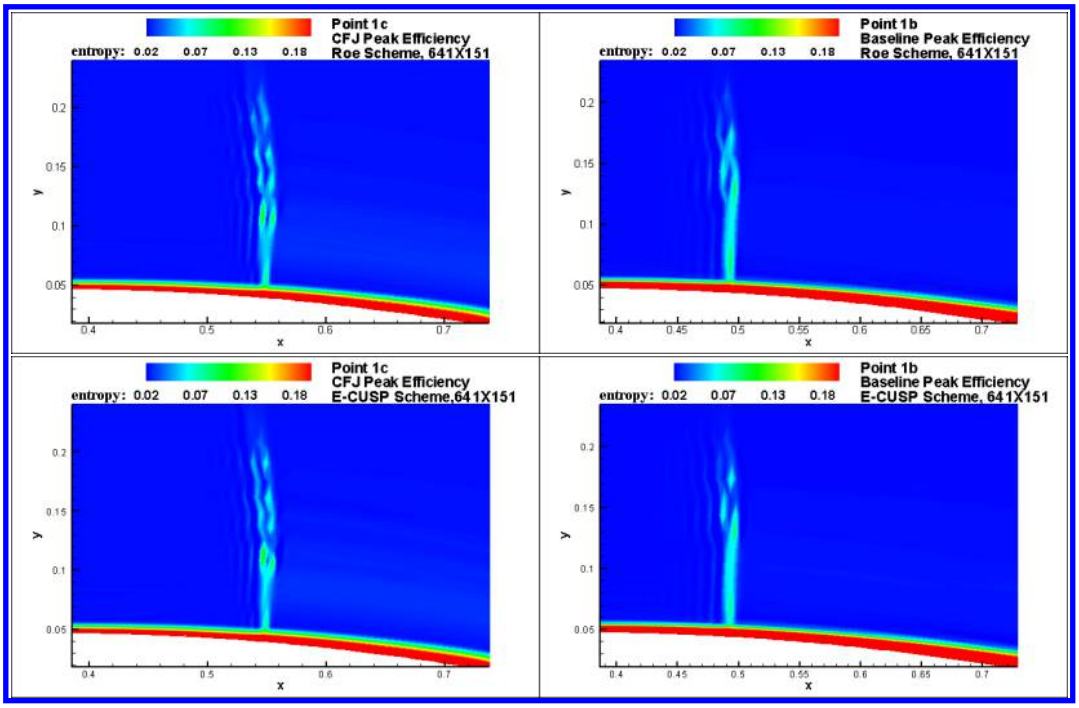

Figure 31: Shock entropy increase captured using Roe scheme and the E-CUSP scheme for the CFJ airfoil and the baseline airfoil at the peak efficiency condition using 641×151 mesh.

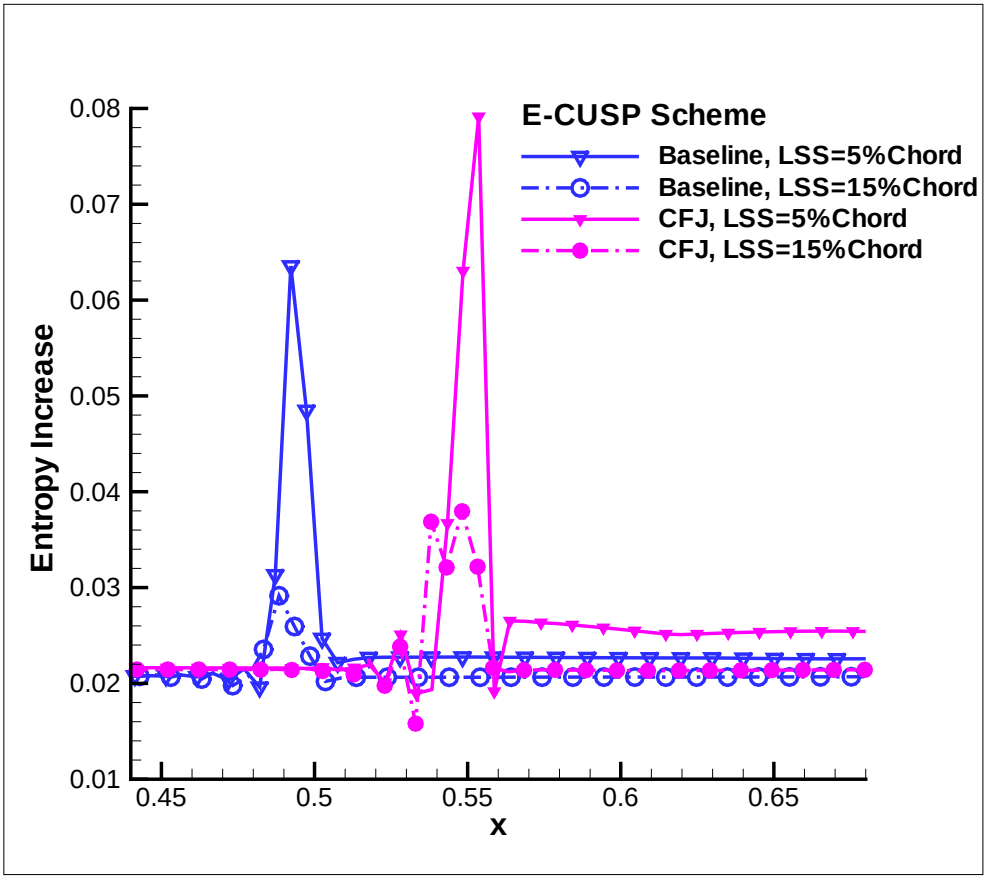

Figure 32: Shock entropy increase distributions at locations above suction surface(LSS) for the CFJ airfoil and the baseline airfoil at the peak efficiency condition.

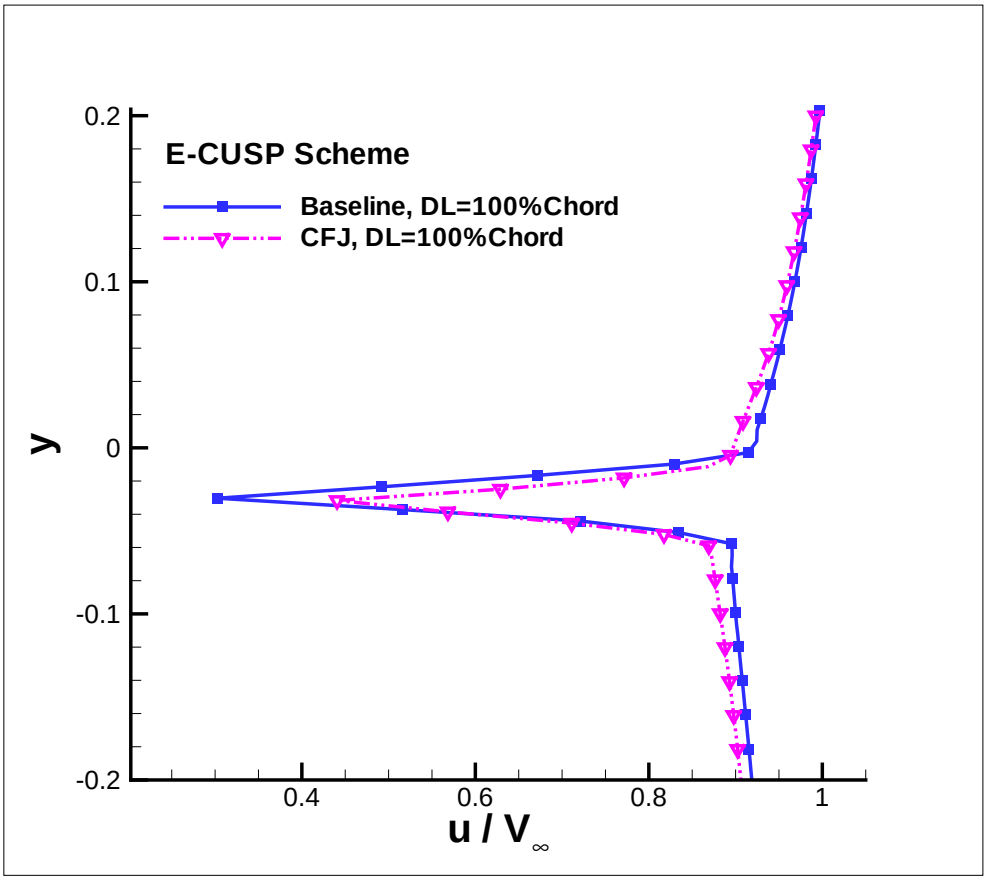

Figure 33: Wake x-component velocity distribution at one chord length downstream location(DL) for the CFJ airfoil and the baseline airfoil at the peak efficiency condition.

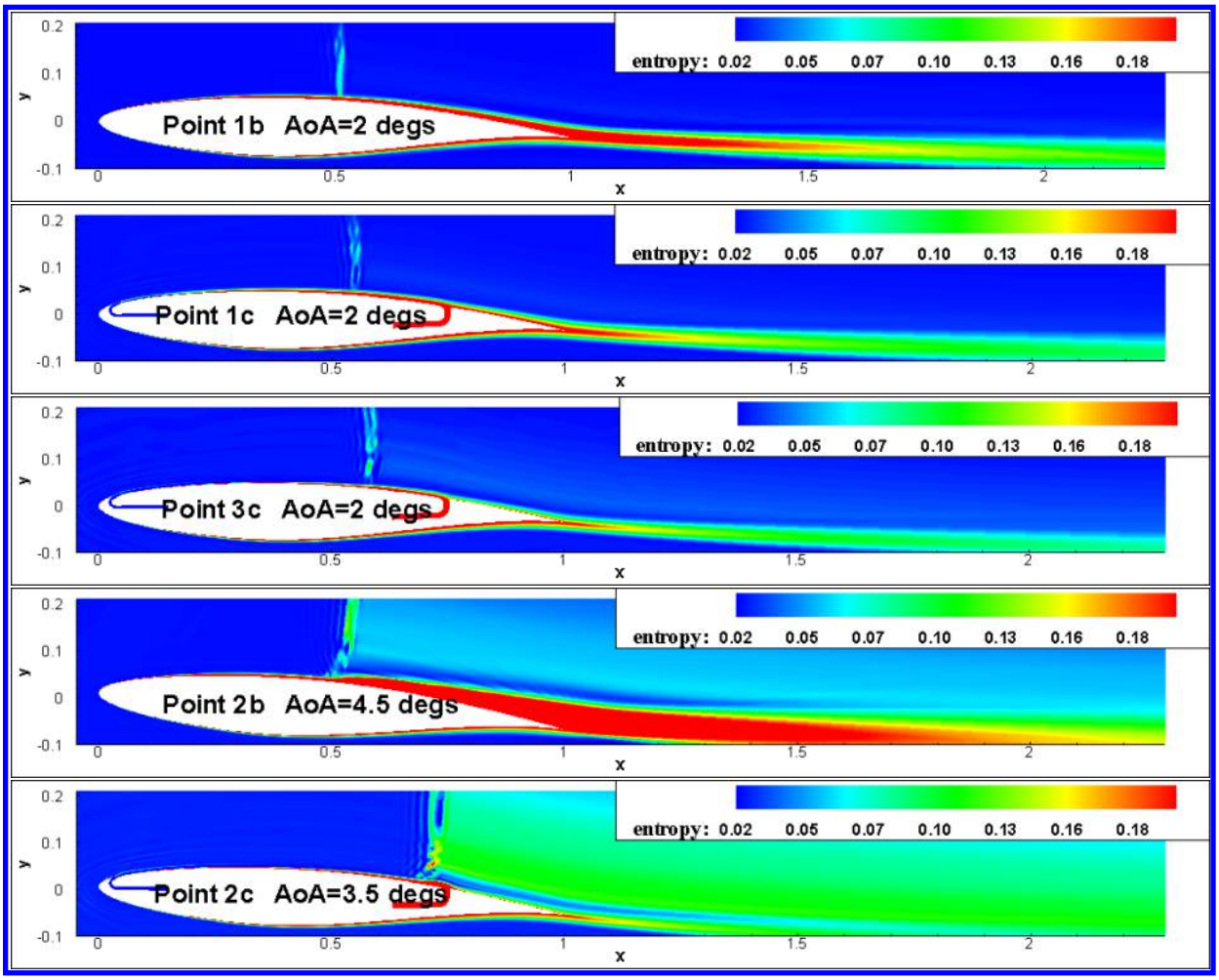

Figure 34: Entropy increase contours comparison for all the characteristics points.

IV. Conclusions

This paper performs a numerical proof of concept study to enhance transonic supercritical airfoil cruise performance using Co-Flow Jet active flow control technique. It is found that the CFJ active flow control can significantly enhance the aerodynamic performance of transonic supercritical airfoil for both lift coefficient C_L and aerodynamic efficiency $(\frac{L}{D})_c$ that includes the CFJ pumping power. For the free-stream condition of M_∞=0.729, Re_∞=6.5 $\times$ 10^6, and AoA from 0° to 5.5°, the CFJ RAE2822 airfoil is able to achieve a performance enhancement with both C_L and $(\frac{L}{D})_c$ increased simultaneously by 18.7% and 14.5%, respectively at the peak aerodynamic efficiency point. At the maximum lift coefficient point, the CFJ airfoil is able to increase the C_L from 0.93 to 1.16 by 25.6% while slight decreasing the $(\frac{L}{D})_c$ from 21.3 to 19.6. Alternatively, with a small increase of aerodynamic efficiency $(\frac{L}{D})_c$ by 2.7%, the CFJ airfoil achieves an increase of C_L by 30.1%. Rigorous mesh refinement study is conducted to ensure solution convergence of the numerical results. Since the baseline airfoil drag is over-predicted by more than 30% due to the inadequacy of the RANS model, the predicted improvement of the CFJ airfoil tends to be on the conservative side.

Several factors affecting the CFJ airfoil performance at transonic flow regime are observed. First, the CFJ flow control can increase the suction surface flow velocity by injection and suction arrangement to increase the circulation around the airfoil; Second, the CFJ flow control is able to push shock wave significantly more downstream and still maintain the maximum Mach number less than 1.3 to achieve near isentropic effect. The substantially enlarged supersonic region on suction surface has a large contribution on lift augment. Third, CFJ is effective on reducing the flow separation caused by the normal shock wave-boundary layer interaction. Fourth, the injection jet velocity is found to be very effective at the magnitude substantially smaller than the freestream velocity, such as half of the freestream velocity. Fifth, a very small jet momentum coefficient with very low energy expenditure is effective and is the key to achieve high cruise aerodynamic efficiency of $(L/D)_c$. Sixth, the CFJ airfoil performance is strongly affected by the the geometry configurations including the suction surface translation amount, injection and suction slot size, location, and orientation.

The CFJ airfoil studied in this paper is based on an existing high performance supercritical airfoil designed using conventional aerodynamics methodology. It is believed that a customer tailored airfoil geometry based on CFJ flow control would achieve even better performance. The unique feature of the CFJ airfoil to augment lift and reduce drag at low energy expenditure shows a great potential to radically improve the transonic airfoil cruise performance when the flow is benign at low AoA. The performance enhancement of CFJ transonic airfoil needs to be further proved by wind tunnel experiment as the next step. It is hoped that this research will open a door to significantly enhance transonic supercritical airfoil performance.

Acknowledgments

The authors would like to acknowledge the computing resource provided by the Center of Computational Sciences at the University of Miami.

References

[1] R. T. Whitcomb. Review of NASA Supercritical Airfoils. *ICAS PAPER 74-10*, 1974.

[2] John Stack. Tests of Airfoils Designed to Delay the Compressibility Burble. *NASA TM*, 976, 1944.

[3] Ira H. Abbott and A. E. Von Doenhoff and Louis S. Jr. Stivers. Summary of Airfoil Data. *NACA Report*, 824, 1945.

[4] R. T. Whitcomb and L. R. Clark. An Airfoil Shape for Efficient Flight at Supercritical Mach Numbers. *NASA TM*, X-1109, 1965.

[5] C.D. Harris. NASA Suprecritical Airfoils. *NASA Technical Paper*, 2969, 1990.

[6] Richard Barnwell. Passive Drag Control of Airfoils at Transonic Speeds. *United States Patent*, 4522360, 1985.

[7] H. Ogawa and H. Babinsky. Shock-Wave/Boundary-Layer Interaction Control Using Three-Dimensional Bumps for Transonic Wings. *AIAA Journal*, 46:1442–1452, 2008.

[8] G. Liu, Y. Tao, Q. Guo and Y. Sun. Transonic Drag Reduction with Contour Bump on a Supercritical Airfoil. *International Conference on Intelligent System Design and Engineering Applications*, 2012.

[9] L. G. Pack and N. W. Schaeffler and C. S. Yao. Active Control of Separation from the Slat Shoulder of a Supercritical Airfoil. *AIAA Journal*, 3156:1142–1149, 2002.

[10] L. P. Melton and C. S. Yao. Active Control of Separation from the Flap of a Supercritical Airfoil. *AIAA Journal*, 44:34–41, 2006.

[11] Louis N. Cattafesta III and Mark Sheplak. Actuators for Active Flow Control. *Annu. Rev. Fluid Mech.*, 43, 2011.

[12] G.-C. Zha and D. C. Paxton. A Novel Flow Control Method for Airfoil Performance Enhancement Using Co-Flow Jet. *Applications of Circulation Control Technologies*, Chapter 10, p. 293-314, Vol. 214, Progress in Astronautics and Aeronautics, AIAA Book Series, Editors: Joslin, R. D. and Jones, G.S., 2006.

[13] G.-C Zha and C. Paxton and A. Conley and A. Wells and B. Carroll. Effect of Injection Slot Size on High Performance Co-Flow Jet Airfoil. *AIAA Journal*, 43, 2006.

[14] G.-C. Zha and W. Gao and C. Paxton. Jet Effects on Co-Flow Jet Airfoil Performance. *AIAA Journal, No. 6*, 45:1222–1231, 2007.

[15] G.-C Zha and B. Carroll and C. Paxton and A. Conley and A. Wells. High Performance Airfoil with Co-Flow Jet Flow Control. *AIAA Journal*, 45, 2007.

[16] Wang, B.-Y. and Haddoukessouni, B. and Levy, J. and Zha, G.-C. Numerical Investigations of Injection Slot Size Effect on the Performance of Co-Flow Jet Airfoil . *AIAA Journal of Aircraft*, 45:2084–2091, 2008.

[17] B. P. E. Dano, D. Kirk, and G.-C. Zha. Experimental Investigation of Jet Mixing Mechanism of Co-Flow Jet Airfoil. AIAA Paper 2010-4421, 5th AIAA Flow Control Conference, Chicago, IL,, 28 Jun - 1 Jul 2010.

[18] B. P. E. Dano, G.-C. Zha, and M. Castillo. Experimental Study of Co-Flow Jet Airfoil Performance Enhancement Using Micro Discreet Jets. AIAA Paper 2011-0941, 49th AIAA Aerospace Sciences Meeting, Orlando, FL,, 4-7 January 2011.

[19] Lefebvre, A. and Dano, B. and Di Franzo, M. and Bartow, W. and Zha, G.-C. Performance of Co-Flow Jet Flow Airfoil with Variation of Mach Number. AIAA Paper 2013-0490, 51st AIAA Aerospace Science Meeting, Grapevine, TX, 7-10 Jan. 2013, to appear in Journal of Aircraft, 2016.

[20] Lefebvre, A. and Zha, G.-C. Numerical Simulation of Pitching Airfoil Performance Enhancement Using Co-Flow Jet Flow Control. AIAA Paper 2013-2517, 31st AIAA Applied Aerodynamics Conference, San Diego, CA, 24 - 27 June 2013.

[21] Lefebvre, A. and Zha, G.-C. . Design of High Wing Loading Compact Electric Airplane Utilizing Co-Flow Jet Flow Control. AIAA Paper 2015-0772, AIAA SciTech2015: 53nd Aerospace Sciences Meeting, Kissimmee, FL, 5-9 Jan 2015.

[22] P.R. Spalart and S.R. Allmaras. A One-equation Turbulence Model for Aerodynamic Flows. AIAA-92-0439, 1992.

[23] G.-C. Zha, Y. Shen, and B. Wang. An improved low diffusion E-CUSP upwind scheme . *Journal of Computer & Fluids*, 48:214–220, 2011.

[24] P. Roe. Approximate Riemann Solvers, Parameter Vectors, and Difference Schemes. *Journal of Computational Physics*, 43:357–372, 1981.

[25] Shen, Y.-Q. and Zha, G.-C. and Wang, B.-Y. Improvement of Stability and Accuracy of Implicit WENO Scheme. *AIAA Journal*, 47, No. 2:331–344, 2009.

[26] Shen, Y.-Q. and Zha, G.-C. and Chen, X.-Y. High Order Conservative Differencing for Viscous Terms and the Application to Vortex-Induced Vibration Flows. *Journal of Computational Physics*, 228(2):8283–8300, 2009.

[27] Y.-Q. Shen, B.-Y. Wang, and G.-C. Zha. Implicit WENO Scheme and High Order Viscous Formulas for Compressible Flows . AIAA Paper 2007-4431, 2007.

[28] B.-Y. Wang and G.-C. Zha. A General Sub-Domain Boundary Mapping Procedure For Structured Grid CFD Parallel Computation. *AIAA Journal of Aerospace Computing, Information, and Communication*, 5, No.11:2084–2091, 2008.

[29] Y.-Q. Shen and G.-C. Zha. Comparison of High Order Schemes for Large Eddy Simulation of Circular Cylinder Flow. AIAA-2009-0945, 47th AIAA Aerospace Sciences Meeting and Exhibit, Orlando, FL, Jan. 5-8, 2009.

[30] Y.-Q. Shen J.-Y. Gan and G.-C Zha. Comparison of Drag Prediction Using RANS models and DDES for the DLR-F6 Configuration Using High Order Schemes. 54th Aerospace Sciences Meeting, San Diego, CA, AIAA Paper 2016-0553, 2016.

[31] Wang, B. Y and Zha, G.-C. Detached-Eddy Simulation of a Co-Flow Jet Airfoil at High Angle of Attack. *AIAA Journal of Aircraft*, 48, 5:1495–1502, 2011.

[32] Im, H.-S. and Zha, G.-C. and Dano, B. P. E. Large Eddy Simulation of Coflow Jet Airfoil at High Angle of Attack. *Journal of Fluid Engineering*, 136(2):021101, 2014.

[33] M. A. McDonald P. H. Cook and M. C. P. Firmin. AEROFOIL RAE 2822: PRESSURE DISTRIBUTIONS, AND BOUNDARY LAYER AND WAKE MEASUREMENTS. *AGARD Advisory Report*, 138-A6:1–77, 1979.

[34] CD-dapco. Validation of STAR-CCM+ for External Aerodynamics in the Aerospace Industry.

[35] H. Namgoong. AIRFOIL OPTIMIZATION FOR MORPHING AIRCRAFT. *PhD Thesis, Purdue University*, 2005.

[36] G.-C Zha, B. Carroll, C. Paxton, A. Conley, and A. Wells. High Performance Airfoil with Co-Flow Jet Flow Control. AIAA-Paper-2005-1260, AIAA the 43rd Aerospace Sciences Meeting and Exhibit Conference, Reno, NV, Jan. 10-13, 2005.